THE ASTROPHYSICAL JOURNAL, 471:930–948, 1996 November 10

ILLUMINATION IN SYMBIOTIC BINARY STARS: NON-LTE PHOTOIONIZATION MODELS. I. HYDROSTATIC CASE

DANIEL PROGA, SCOTT J. KENYON, AND JOHN C. RAYMOND
Harvard-Smithsonian Center for Astrophysics, 60 Garden Street, Cambridge, MA 02138; dproga, skenyon, jraymond @cfa.harvard.edu.
AND
JOANNA MIKOŁAJEWSKA
Copernicus Astronomical Center, Bartycka 18, PL 00-716 Warsaw, Poland; joanna_mikolajewska@camk.edu.pl
Received 1995 November 20; accepted 1996 May 21

ABSTRACT

We describe a non-LTE photoionization code that calculates the atmospheric structure and emergent spectrum of a red giant illuminated by the hot component of a symbiotic binary system. The model assumes hydrostatic, radiative, and statistical equilibrium for the red giant atmosphere and solves the radiative transfer equation with a local escape probability method. We compute non-LTE level populations for a variety of ions and predict the variation of emission-line fluxes as function of the temperature and luminosity of the hot component.

Our models produce strong emission lines only when the hot component has a high effective temperature, $T_h \gtrsim 100{,}000$ K, for hot component luminosities, $L_h \gtrsim 630\ L_\odot$. Predicted electron densities and temperatures for the photoionized atmosphere agree with observations. The models also produce reasonably large continuum variations that are consistent with the light curves of some symbiotic stars. However, predictions for most optical and ultraviolet emission-line fluxes fall well below those observed in typical symbiotic stars. We conclude that the hot component must illuminate a red giant wind to reproduce observed line fluxes. Hydrostatic red giant atmospheres simply do not have enough material beyond the photosphere to account for the emission features observed in most symbiotics.

Illumination can modify the structure of a red giant atmosphere even when the emitted spectrum changes very little. Energetic photons from the hot component cause the atmosphere to expand by several percent for large hot component luminosities. This expansion is insufficient to increase the red giant mass-loss rate, except in systems where the giant already fills or nearly fills its Roche lobe.

Subject headings: binaries: symbiotic — radiative transfer — stars: emission-line, Be — stars: late-type

1. INTRODUCTION

Many binary systems have light curves that display the "reflection effect," in which one binary component heats up the facing hemisphere of its companion. The higher effective temperature of the heated hemisphere produces a characteristic sinusoidal light variation observed in Algol binaries, precataclysmic binaries, cataclysmic binaries, and symbiotic stars (e.g., Grauer & Bond 1983; Kenyon 1982). This illumination is important when the radii of the component stars are a few percent of the orbital separation, even if the stars have similar effective temperatures (Vaz 1984; Vaz & Nordlund 1985). The most spectacular reflection effects occur when the effective temperatures of the component stars are vastly different. For example, many precataclysmic binaries have 0.5–1.0 mag optical continuum variations and strong, narrow H I, He I, and He II emission lines that vary in phase with the spectroscopic orbit (e.g., Margon, Downes, & Katz 1981; Grauer & Bond 1983; Catalán et al. 1994). The bright continuum and emission lines are best interpreted as extreme-ultraviolet (EUV) radiation from a white dwarf star reprocessed by the illuminated hemisphere of the red dwarf companion (e.g., Catalán et al. 1994; Ferguson & James 1994).

Illumination also changes the atmospheric structure of the heated star. The extra continuum and line emission distorts absorption line profiles and thus alters orbital velocity curves. Differential heating across the stellar surface also sets up horizontal pressure differences that can drive horizontal energy transfer (Vaz & Nordlund 1985; Brett & Smith 1993). In some cases, the heated atmosphere expands, which leads to additional mass loss (Podsiadlowski 1991; Tavani & London 1993).

Many symbiotic binaries have reflection light curves (Kenyon 1986). In these systems, a hot component with $T_h \sim 10^5$ K heats the outer atmosphere of its red giant companion (see the top panel of Fig. 1). Merrill (1959, and references therein) first noted emission-line and continuum variations in phase with the 800 day orbit of AG Peg. Belyakina (1968a, 1968b, 1970) confirmed these observations and interpreted the data with a simple reflection model. Recent studies confirm illumination heating in many symbiotics (e.g., Munari 1988). Although some high-ionization emission lines form near the hot component, a substantial fraction of the H I and He I emission forms in or close to the red giant photosphere (e.g., Kenyon et al. 1993 Dobrzycka, Kenyon, & Mikołajewska 1993; Mikołajewska et al. 1995). This region has the high density, $n_e \sim 10^9$–10^{11} cm^{-3}, and the low thermal velocity, $v \approx 10$–20 km s^{-1}, expected for the upper atmosphere of a red giant. Radiation from the hot component also preferentially fills in short-wavelength absorption bands on the heated red giant atmosphere, which results in a variation of TiO band strengths with orbital phase and wavelength (e.g., Mikołajewska, Kenyon, & Mikołajewski 1989).

In addition to producing bright emission lines, illumination might change the overall structure of the red giant in a symbiotic binary. Kenyon & Gallagher (1983; see also Kenyon 1988) first suggested that illumination might

increase the red giant mass-loss rate in systems where the giant underfills its tidal lobe. Munari & Renzini (1992; see also Munari 1988) expanded this idea. They noted that additional mass loss might produce a feedback mechanism in which the hot component regulates the structure of the red giant's atmosphere and mass-loss rate. A substantial increase in the red giant mass-loss rate shortens the lifetime of a symbiotic binary and might have important consequences for galactic binary evolution models (see Yungel'son et al. 1995, and references therein).

This paper begins a theoretical study of illumination in symbiotic binary systems. Our goals are to derive continuum and emission-line fluxes for comparison with observations and to estimate the importance of illumination in the evolution of the red giant primary star. We describe the calculation and initial results in §§ 2.1–2.4 and compare our predictions with some observations in § 2.5. We conclude with a brief discussion and summary in § 3.

2. MODELS

2.1. *Background*

Most stellar atmosphere models rely on several basic assumptions to determine the emergent flux from a stellar photosphere. These "classical" models generally adopt hydrostatic equilibrium, parallel symmetric stratification, local thermodynamic equilibrium (LTE), and an energy equilibrium that includes only the radiative flux and a convective flux approximated with the mixing-length theory. As more opacity sources are added to the radiative equilibrium calculation, classical atmosphere models more closely reproduce spectra for most normal main-sequence and red giant stars (e.g., Kurucz 1991; Brown et al. 1989).

Physical treatments of illumination usually adopt classical atmosphere assumptions and simply include an incident, plane-parallel radiation field. For example, Vaz & Nordlund (1985) and Nordlund & Vaz (1990) studied reflection in Algol binaries using a modified version of the Uppsala Model Atmosphere (UMA) code (Gustafsson et al. 1975). Brett & Smith (1993) investigated the irradiation of the secondary star in a dwarf nova binary with a code developed for red dwarf atmospheres (Brett 1989). Both groups also studied horizontal energy transfer in convective models in an approximate one-dimensional manner.

Classical atmosphere models are, however, too simplistic to explain many observations of red giant stars (see Gustafsson & Jørgensen 1994, and references therein). Chromospheric emission from Mg II, Ca II, and more highly ionized species require acoustic or magnetic heating to raise the temperature above the photosphere (e.g., Jordan & Linsky 1987). Modest mass-loss rates invalidate the assumption of hydrostatic equilibrium; higher mass-loss rates require spherically symmetric models instead of plane-parallel models. Shocks from pulsations extend the atmosphere and can also produce strong emission lines (e.g., Bowen 1988). The basic LTE assumptions for radiative transfer break down in most of these situations due to the high temperature and low density of the emitting region. Non-LTE calculations improve the ability of models to reproduce the data, but a complete theory for red giant atmospheres does not yet exist (Gustafsson & Jørgensen 1994).

Figure 1 outlines the basic philosophy of our model atmosphere calculations. The top panel illustrates the basic

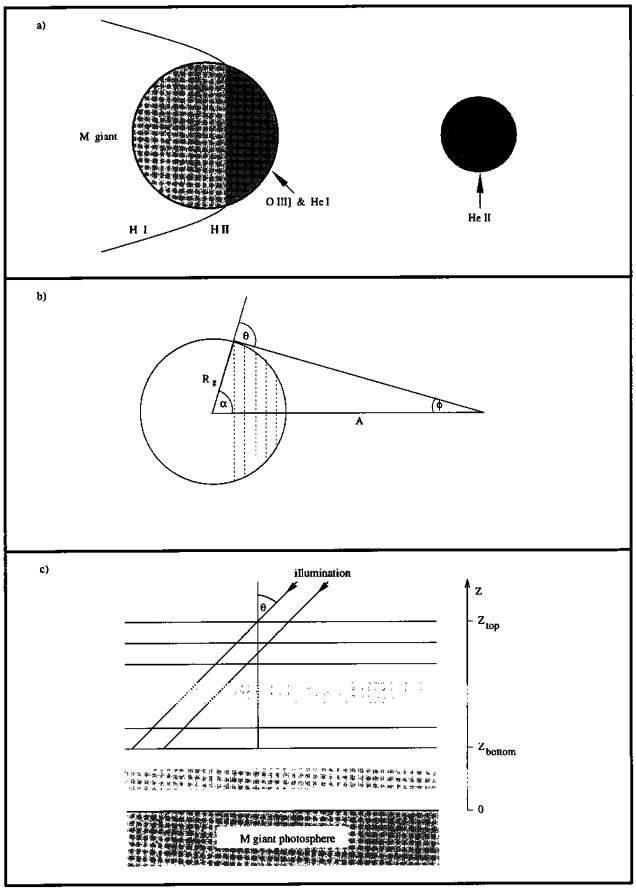

FIG. 1.—Schematic illustration of a symbiotic binary with illumination. (*a*) The basic geometry of the binary, in which a hot, compact star photoionizes a wind from a red giant companion and illuminates the companion's facing hemisphere. A dense He^{++} region surrounds the hot component. Lower ionization emission is produced in a H^+ zone between the two stars and in the illuminated red giant atmosphere. Neutral material lies behind the giant in a region shielded from the hot component. (*b*) An idealized geometry, in which a hot point source irradiates a spherical giant without a wind. We assume the illumination is constant in concentric annuli, shown as dashed lines, centered on the substellar point of the red giant atmosphere as viewed from the hot component. For each concentric annulus, the hot component flux strikes the surface of the red giant atmosphere at an angle θ with respect to the normal to the surface. (*c*) The framework of our one-dimensional calculations for an individual annulus. We assume a plane-parallel atmosphere illuminated by a plane-parallel radiation field at the incident angle θ. We consider the upper part of the atmosphere with height z_{top}. Our calculations stop at a height, z_{bottom}, at which all ionizing photons are absorbed.

geometry of a symbiotic binary, in which a hot, compact star photoionizes a wind from a red giant companion and illuminates the companion's facing hemisphere. To compute the atmospheric structure, we specify the separation, A; the red giant mass, M_g, radius, R_g, and effective temperature, T_g; and the hot component luminosity, L_h, and effective temperature, T_h (see Table 1). The middle panel approximates reality with a hot point source irradiating a spherical giant without a wind. We assume that illumination is constant in concentric annuli centered on the substellar point of the red giant atmosphere as viewed from the hot component. For each concentric annulus, the hot component flux strikes the surface of the red giant atmosphere at an angle θ with respect to the normal to the surface. The flux of the illuminated red giant hemisphere is the sum of contributions from each annulus.

TABLE 1

MODEL ASSUMPTIONS

Component	Red Giant	Hot Component
Atmosphere	Hydrostatic equilibrium Radiative equilibrium Non–LTE	...
Wind	No	No
Photospheric radiative field	Plane-parallel Planck distribution	Plane-parallel Planck distribution

The bottom panel of Figure 1 shows the framework of our one-dimensional calculations for an individual annulus. We assume a plane-parallel atmosphere illuminated by a plane-parallel radiation field at an incident angle θ. This atmosphere is in hydrostatic, radiative, and statistical equilibrium. We also assume that both stars radiate as blackbodies. We abandon LTE because the hot component emits most of its flux shortward of the Lyman limit, and the $\tau_{912} = 1$ surface lies many scale heights above the red giant's optical photosphere. The ionization balance and level populations in this region are not well described by local conditions due to the low density and the incident radiation field from a much hotter star.

Our idealized geometry provides a strict lower limit to the emission-line flux in a symbiotic binary. A red giant with $R_g \sim 100\ R_\odot$ intercepts roughly 1%–2% of the total hot component flux for a typical separation, $A \sim 2$–3 AU. Most symbiotic hot components have $L_h \sim 10^3\ L_\odot$ (Kenyon & Webbink 1984; Mürset et al. 1991; Morgan 1992); the red giant can then absorb and reradiate a luminosity of 10–20 $L_\odot$ under normal circumstances. If the giant reemits *all* this flux in emission lines, we expect an Hβ line flux of $F(\mathrm{H}\beta) \lesssim 3 \times 10^{-12}$ ergs cm^{-2} s^{-1} for a distance of $\sim$1 kpc (Osterbrock 1989). This estimate falls well below the observed flux of a typical system, ~ 1–10×10^{-11} ergs cm^{-2} s^{-1} (e.g., Kenyon et al. 1993; Mikołajewska et al. 1995). We can increase the predicted illumination flux by increasing the solid angle of the red giant atmosphere, $\Omega = (R_g/2A)^2$. Roche geometry limits the size of the red giant photosphere to $R_g/A \sim \frac{1}{2}$, which increases our upper limit for $F(\mathrm{H}\beta)$ only by a factor of 4. Adding a wind allows the red giant atmosphere to absorb a much larger fraction of the hot component flux. A mass-loss rate of $\sim 10^{-7}\ M_\odot$ yr^{-1} is usually sufficient to explain the Hβ flux and radio emission in most systems (e.g., Seaquist, Krogulec, & Taylor 1993).

We develop our hydrostatic illumination model in the following sections and will consider wind models in a subsequent paper.

2.2. *Calculations*

Our photoionization code is an improved version of Raymond's (1993; see also Raymond & Smith 1977) X-ray illumination code, which calculates the spectrum of an irradiated accretion disk in a low-mass X-ray binary system. We assume a plane-parallel red giant atmosphere in hydrostatic equilibrium illuminated by an external blackbody radiation field. We separate this atmosphere into the photosphere and an "upper" part where the Rosseland mean optical depth is $\tau_{\mathrm{Ross}} \leq 0.3$. Our calculation divides the upper atmosphere into 200 layers with constant geometric thickness, Δz (see the bottom panel of Fig. 1), and it solves iteratively for the emergent radiation field and the equilibrium density and temperature structure. We adopt an escape probability method to solve the radiative transfer equation in 500 logarithmically spaced bins covering photon energies 0.01 eV $\leq h\nu \leq 1$ keV with an energy resolution of $\log \delta(h\nu) = 0.01$. We consider a variety of atomic processes in the upper atmosphere, as described in Appendix A, for the elements listed in Table 2. Proga, Mikołajewska, & Kenyon (1994) describe our adopted He I atomic model and rates; Raymond (1993) summarizes the atomic models and rates for all other elements. This calculation does not include molecules. Thus, we do not consider how the external radiation field changes the structure of the red giant photosphere.

To derive a hydrostatic and radiative equilibrium model for the illuminated atmosphere, we calculate the structure from the top of the temperature, z_{top}, to the point where 99% or more of the incident flux with $\lambda \leq 912$ Å has been absorbed, z_{bottom}. Each iteration consists of two steps. We solve first for the temperature, the level populations of each ionization state of twelve elements, and the radiation field using energy balance and the local escape probability. For each new temperature structure, we then integrate the hydrostatic equilibrium equation to derive a new density structure. This process repeats until the density converges to the 1% level, which usually requires 20–100 iterations. Additional iterations change the density/temperature structure near the photosphere by less than 5%, which modifies the resulting spectrum by less than 5%. The final one-dimensional model predicts the temperature and density structure with z and the line and continuum emission. We assume that radiation from the red giant photosphere does not interact with the upper atmosphere and simply add this flux to the upward propagating flux from the illuminated upper atmosphere. This approximation is reasonable because a red giant emits very little flux where the upper atmosphere has significant optical depth. Appendix A describes additional details of the model calculations.

TABLE 2

ELEMENTS AND ABUNDANCES USED

Element	Abundance
H	12.00
He	10.99
C	8.56
N	8.05
O	8.93
Ne	8.09
Mg	7.58
Si	7.55
S	7.21
Ar	6.56
Ca	6.36
Fe	7.67

The total flux of the illuminated red giant hemisphere is the sum of contributions from each annulus. A complete solution thus requires models for different incident angles, $0 \leq \theta \leq \theta_{\max}$ (see Fig. 1). First we consider models at a representative incident angle, θ_r, for which the effective temperature of the illuminated annulus is equal to the effective temperature of the whole illuminated red giant hemisphere (see Appendix B). This approach reduces the number of intermediate calculations and allows us to concentrate on the properties of models as functions of L_h and T_h. We define a second parameter, β, to measure the strength of the illuminating radiation field relative to that of the giant at $\theta = 0°$:

$$\beta = \frac{R_g^2}{A^2}\frac{L_h}{L_g}, \quad (1)$$

We expect significant changes in the structure of the red giant atmosphere for $\beta \gg 1$ and negligible changes when $\beta \ll 1$. All calculations assume $T_g = 3600$ K, $R_g = 85\ R_\odot$, $L_g \approx 1100\ L_\odot$, and $M_g = 2.5\ M_\odot$ for the red giant and a binary separation, $A = 3$ AU, which are typical parameters for symbiotic stars (Kenyon 1986).

Illumination divides the atmosphere into three main regions: an undisturbed lower atmosphere, a photoionized upper atmosphere, and a thin transition region where ionized species recombine to neutral states. Figure 2 illustrates this structure for $T_h = 2 \times 10^5$ K and $L_h = 6.2 \times 10^4\ L_\odot$ ($\beta = 1$; $\theta_r = 64°$). This luminosity is too large for a typical quiescent symbiotic star but could represent some extreme systems in outburst (Mikołajewska & Kenyon 1992). Photoionization of He II and H I heats the upper atmosphere to $\sim 2.8 \times 10^4$ K for $z > 1.75 \times 10^{11}$ cm (Fig. 2*a*). The temperature gradually declines to $\sim 2.3 \times 10^4$ K at $z = 1.5 \times 10^{11}$ cm and then decreases rapidly to $\sim 1.6 \times 10^4$ K at $z = 1.43 \times 10^{11}$ cm due to an increase in recombination and line cooling at higher density. At $z = 1.43 \times 10^{11}$ cm, He III recombines. The photoionization of H I is then the most important heating source (see Figs. 2*c*–2*d*), and the emission lines become optically thick. The temperature jumps by ~ 500 K at this point because the optically thick emission lines do not cool the atmosphere as efficiently. The temperature decreases gradually to $\sim 1.4 \times 10^4$ K at $z = 1.34 \times 10^{11}$ cm and then drops abruptly to $\sim 2.4 \times 10^3$ K. At this depth, all the ionizing radiation has been absorbed and the ions recombine. The transition from a normal red giant atmosphere to a photoionized atmosphere thus occurs at $z_{\rm bottom} = 1.34 \times 10^{11}$ cm. The temperature and density structure follow the nonilluminated structure below this point.

The density variations in the atmosphere mirror the temperature changes (Fig. 2*b*). The logarithm of the hydrogen density decreases almost linearly with z in the undisturbed part of the atmosphere because the temperature is almost constant. At $z = z_{\rm bottom}$, the temperature increases by a factor of ~ 6, and the mean molecular weight decreases by a factor of ~ 2. The density then falls by a factor of ~ 10 to maintain pressure balance. A second steep density drop occurs at the transition from He II to He III, $z = 1.43 \times 10^{11}$ cm, when the temperature also decreases sharply. The density then maintains a fairly flat profile out to the top of the atmosphere. The electron density is always a factor of 1.1–1.2 larger than the hydrogen density in regions where hydrogen is nearly completely ionized and drops dramatically when hydrogen recombines (Fig. 2*b*; *dashed line*).

Figures 2*c* and 2*d* show the fractional populations of H and He. Solid lines represent the ground states of neutral H I and He I; dashed lines represent H II and He III. In Figure 2*d*, the dotted line corresponds to the ground state of He II. The three distinct He regions in Figure 2*d* correspond

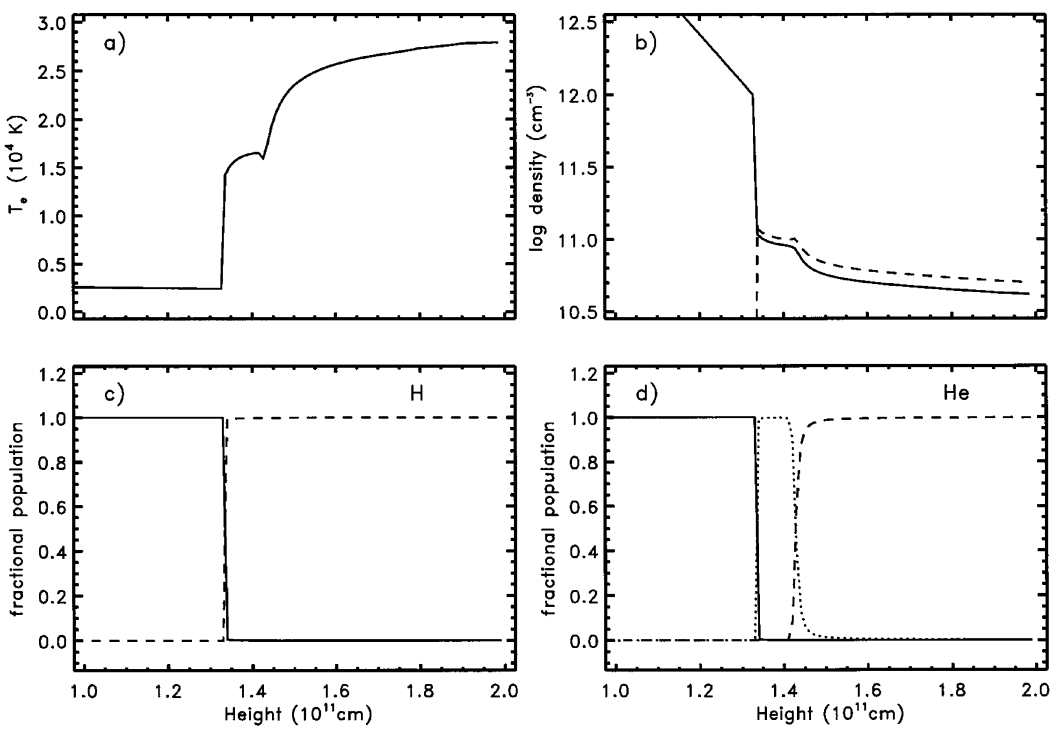

FIG. 2.—Model atmosphere structure for $T_h = 2 \times 10^5$ K and $\beta = 1$. (*a*) T_e radial profile. (*b*) Hydrogen and electron number density profiles (*solid and dashed lines*). (*c*) Fractional population of the ground level of H I and H II (*solid and dashed lines*). (*d*) Fractional population of the ground level of He I, He II, and He III (*solid, dotted, and dashed lines*).

to the three different temperature structures in Figure 2*a*. The He III region is hotter than the He II region due to the higher energy of the ionizing photons. The temperature gradient is also steeper in the He III region because the region is optically thin to most emission lines. In contrast, the He II region is optically thick in the most important coolants and has a flatter temperature gradient.

Figure 3 compares the reprocessed spectrum, $J^u(\lambda)$, with the incident flux, $J^{in}_{0,r}(\lambda)$, and the blackbody spectrum of the undisturbed red giant, $B(\lambda, T_g)$. Radiation from the red giant (*dot-dashed line*) dominates for $\lambda > 4000$ Å. The "hot" incident flux (*dashed line*) dominates at short wavelengths, $\lambda < 500$ Å. The reprocessed flux (*solid line*) dominates at intermediate wavelengths, where the flux from the two stellar components is weak. Reprocessing produces prominent Lyman and Balmer continua and emission lines from Lα, C IV λ1550, O V] λ1218, and O VI λ1034.

Figure 4 shows the total UV and optical flux of the model (*thick line*) at a distance of 1 kpc. For an orbital inclination of 90° and orbital phase of 0.0 (when the hot component lies in front of the giant), the total spectrum of this model is

$$F(\lambda) = \frac{L_h}{\sigma T_h^4} B(\lambda, T_h) + 4\pi R_g^2 [B(\lambda, T_g) + J^u(\lambda)] . \quad (2)$$

Our model spectrum displays a strong blue continuum, a weaker red continuum, a Balmer emission continuum, several intense UV emission lines, and some weak optical lines. This spectrum generally resembles a *typical* symbiotic star spectrum. We did not include the red giant wind in our calculation; the predicted spectrum thus does not include any forbidden line emission from low-density regions.

Figure 4 also shows blackbody flux curves for a binary without illumination (*dashed line*) and with a simple LTE treatment of illumination (*dotted line*). The dotted curve assumes that the red giant reradiates the incident flux locally at a higher effective temperature as described in Appendix B (eq. [B9]). In this case, the effective temperature of the red giant increases by ~400 K. The simple LTE approximation clearly overestimates the red continuum flux compared to our more detailed non-LTE calculation.

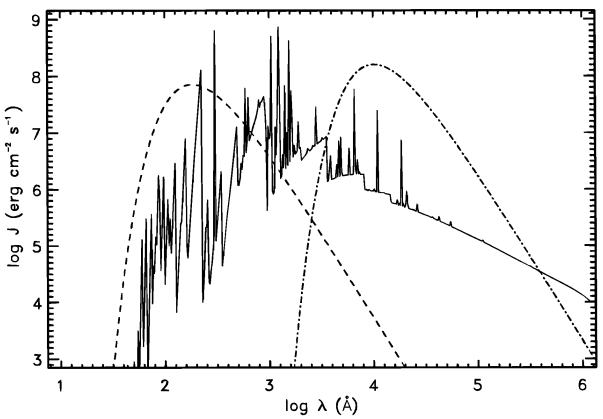

FIG. 3.—Surface fluxes of the model in Fig. 2. Dot-dashed line plots the blackbody spectrum adopted for the red giant; dashed line plots the incident blackbody for the hot component. Solid line indicates the output spectrum of the illumination model described in the text.

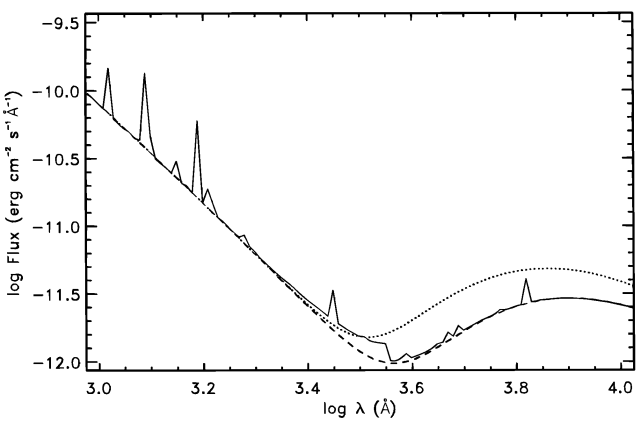

FIG. 4.—The total UV and optical flux of the model (*thick line*), for a distance of 1 kpc, an orbital inclination of 90°, and orbital phase of 0.0 (when the hot component lies in front of the giant). For comparison, the dotted and dashed lines show the two blackbody flux curves for the same parameters without illumination (*dashed curve*) and with LTE illumination (*dotted curve*). LTE illumination assumes that the red giant locally reradiates all incident radiation as a blackbody with a higher effective temperature (in this case by 400 K).

2.3. *Model Grid*

To explore how the line and continuum fluxes of the illuminated atmosphere vary with input parameters, we now consider a grid of models in the (T_h, L_h) plane. Table 3 summarizes salient features of this grid. Columns (1) and (2) list L_h and β; column (3) lists T_h. Other parameters of the grid have the same values as in § 2.2. The input hot component temperatures range from 0.2×10^5 K to 2×10^5 K; the input luminosities span $L_h \sim 6.2 \times 10^2$ $L_\odot$ to 6.2×10^5 $L_\odot$. These parameters are typical of symbiotic stars. For example, Mürset et al. (1991) found 0.55×10^5 K $\leq T_h \leq 2.1 \times 10^5$ K and 0.3 $L_\odot \leq L_h \leq 3.7 \times 10^4$ $L_\odot$ for symbiotics with He II λ1640 emission. Our grid thus matches the observed temperature range of symbiotic stars. We do not consider lower luminosities for the hot component because these cannot modify the red giant atmosphere significantly. Our highest luminosity models are unrealistic for nearly all symbiotics, but these cases provide good tests of our code and verify trends seen at lower luminosities.

Figure 5 compares blackbody flux curves for a binary without illumination with model spectra for all (L_h, T_h) in our grid except $T_h = 0.2 \times 10^5$ K. Model spectra for this low hot component temperature are practically indistinguishable from spectra without illumination. For $T_h = 0.5 \times 10^5$ K, the model spectra display very little continuum emission and a few weak, low-ionization lines such as Lyα and Hβ (Fig. 5*a*). The emission spectrum becomes more prominent as T_h increases because the hot component then emits more ionizing photons. Figure 5*b* shows a richer line spectrum at $T_h = 10^5$ K, with strong H I and He I optical lines and many UV lines. All UV lines weaken with L_h relative to the continuum except Lyα and C IV λ1550. These models produce a noticeable Balmer emission jump only for $L_h \gtrsim 6.2 \times 10^4$ $L_\odot$. The Paschen continuum makes a significant contribution to the red giant continuum only at the highest luminosity, $L_h \gtrsim 6.2 \times 10^5$ $L_\odot$. Spectra of our highest temperature model closely resemble spectra of symbiotic stars (Fig. 5*c*). The UV emission-line spectrum is quite prominent, with very strong H I, He II, C IV, O IV], Si IV, and Mg II UV lines at all luminosities. The C III] λ1908, Si III] λ1892, and Fe II λλ2343, 2403, 2607 lines weaken dramatically, and Mg II λ2800 strengthens relative

TABLE 3

LOGARITHM OF MODEL EMISSION-LINE FLUXES[a]

A. H, He LINES

L_h ($L_\odot$) (1)	β (2)	T_h (10^5 K) (3)	Hα (4)	Hβ (5)	Pα (6)	He I λ3889 (7)	He I λ4471 (8)	He I λ5876 (9)	He I λ6678 (10)	He I λ7065 (11)	He I λ10830 (12)	He II λ1640 (13)	He II λ4686 (14)
6.2×10^2.....	0.01	0.2	−12.9	−13.4	−13.9	−14.9	−15.4	−14.9	−15.5	−15.2	−13.6	−21.3	−22.3
	0.01	0.5	−11.8	−12.3	−12.8	−12.8	−13.2	−12.7	−13.4	−13.0	−11.6	−13.8	−14.8
	0.01	1.0	−11.6	−12.2	−12.7	−12.7	−13.1	−12.6	−13.4	−13.0	−11.5	−12.2	−13.3
	0.01	2.0	−11.6	−12.4	−12.6	−13.3	−13.3	−12.8	−13.7	−13.3	−11.9	−11.7	−12.7
6.2×10^3.....	0.1	0.2	−11.8	−12.4	−12.9	−13.8	−14.3	−13.8	−14.4	−14.1	−12.6	−19.9	−21.0
	0.1	0.5	−10.8	−11.4	−11.8	−11.8	−12.2	−11.7	−12.5	−12.0	−10.6	−12.3	−13.2
	0.1	1.0	−10.5	−11.4	−11.5	−11.7	−12.0	−11.5	−12.4	−11.9	−10.5	−11.2	−12.2
	0.1	2.0	−10.6	−11.7	−11.7	−12.3	−12.7	−12.2	−13.0	−12.6	−11.1	−10.7	−11.8
6.2×10^4.....	1	0.2	−10.7	−11.3	−11.8	−12.8	−13.2	−12.7	−13.4	−13.2	−11.8	−18.5	−19.5
	1	0.5	−9.7	−10.5	−10.6	−10.7	−11.1	−10.5	−11.4	−10.7	−9.8	−11.3	−12.2
	1	1.0	−9.5	−10.3	−10.5	−10.5	−10.9	−10.4	−11.2	−10.6	−9.7	−10.1	−11.0
	1	2.0	−9.7	−10.6	−10.6	−11.0	−11.4	−10.9	−11.8	−11.2	−10.1	−9.7	−10.7
6.2×10^5.....	10	0.2	−9.2	−9.6	−10.2	−11.7	−12.1	−11.6	−12.3	−12.2	−10.9	−16.9	−18.0
	10	0.5	−9.0	−9.4	−9.9	−9.6	−10.2	−9.6	−10.3	−9.8	−9.3	−10.0	−10.8
	10	1.0	−8.9	−9.3	−9.8	−9.4	−9.9	−9.4	−9.9	−9.5	−9.2	−9.1	−9.9
	10	2.0	−9.0	−9.6	−10.0	−9.7	−10.2	−9.7	−10.4	−9.9	−9.4	−8.7	−9.6

B. C, N LINES

L_h ($L_\odot$) (1)	β (2)	T_h (10^5 K) (3)	C II λ1335 (4)	C II] λ2325 (5)	C III] λ1908 (6)	C IV λ1550 (7)	N II] λ2141 (8)	N III] λ1750 (9)	N IV] λ1486 (10)	N V λ1240 (11)
6.2×10^2.....	0.01	0.2	−13.7	−12.8	−15.2		−14.1	−16.6		
	0.01	0.5	−12.5	−12.2	−11.6	−12.9	−13.6	−12.2	−14.0	
	0.01	1.0	−12.3	−12.1	−11.3	−11.1	−13.7	−12.0	−12.3	−13.5
	0.01	2.0	−12.2	−12.1	−11.5	−10.9	−13.7	−12.2	−12.2	−11.9
6.2×10^3.....	0.1	0.2	−12.5	−11.8	−13.7		−13.1	−14.8		
	0.1	0.5	−11.9	−11.9	−10.8	−11.2	−13.4	−11.2	−12.4	−18.2
	0.1	1.0	−11.6	−11.7	−10.7	−9.7	−13.5	−11.2	−11.0	−11.7
	0.1	2.0	−11.6	−11.8	−11.1	−9.7	−13.6	−11.6	−11.2	−10.4
6.2×10^4.....	1	0.2	−11.2	−10.8	−12.4		−12.1	−13.1		
	1	0.5	−10.9	−11.3	−10.0	−9.7	−13.0	−10.1	−11.1	−15.8
	1	1.0	−11.0	−11.5	−10.3	−8.7	−13.7	−10.5	−10.0	−10.0
	1	2.0	−11.1	−11.6	−10.9	−8.8	−13.8	−11.1	−10.5	−9.5
6.2×10^5.....	10	0.2	−10.0	−9.9	−11.4		−11.2	−11.8		
	10	0.5	−10.1	−11.1	−9.3	−8.7	−12.7	−9.2	−10.2	−14.6
	10	1.0	−10.2	−11.4	−9.7	−7.9	−13.6	−9.7	−9.0	−8.8
	10	2.0	−10.2	−11.4	−10.4	−8.0	−13.8	−10.5	−9.7	−8.6

C. O, Mg, Si LINES

L_h (1)	(2)	T_h (3)	O III] (4)	O IV] (5)	O V (6)	O V (7)	O VI (8)	Mg II (9)	Si II] (10)	Si III] (11)	Si IV (12)
6.2×10^2.....	0.01	0.2	−17.6					−13.1	−14.9	−13.3	−19.1
	0.01	0.5	−11.9	−15.0				−12.0	−13.9	−11.5	−12.6
	0.01	1.0	−11.5	−12.3	−13.6	−19.4	−16.3	−11.4	−13.5	−11.5	−11.7
	0.01	2.0	−12.0	−11.7	−11.8	−17.2	−12.7	−12.2	−13.6	−11.9	−11.7
6.2×10^3.....	0.1	0.2	−15.7					−12.6	−14.4	−12.1	−17.2
	0.1	0.5	−10.8	−14.5	−18.6			−11.5	−13.8	−10.6	−11.0
	0.1	1.0	−10.4	−11.1	−11.8	−17.2	−13.8	−10.7	−13.4	−10.9	−10.6
	0.1	2.0	−11.1	−10.6	−10.2	−14.8	−10.3	−11.0	−13.5	−11.2	−10.8
6.2×10^4.....	1	0.2	−14.0					−11.8	−13.9	−10.9	−15.2
	1	0.5	−9.6	−13.6	−18.4			−10.6	−13.5	−9.7	−9.7
	1	1.0	−9.5	−9.9	−10.1	−14.7	−11.4	−10.0	−13.9	−10.4	−9.8
	1	2.0	−10.1	−9.8	−9.0	−13.1	−8.7	−10.1	−13.7	−10.6	−10.0
6.2×10^5.....	10	0.2	−12.6					−10.8	−13.4	−9.7	−13.5
	10	0.5	−8.8	−12.6	−16.0			−10.1	−13.6	−9.1	−8.7
	10	1.0	−8.5	−9.0	−8.8	−12.8	−9.7	−9.3	−14.5	−10.1	−8.8
	10	2.0	−9.1	−9.1	−8.0	−11.3	−7.6	−9.1	−14.1	−10.1	−9.1

NOTE.—Blank spaces mark fluxes practically equal to zero.

[a] In units of ergs cm^{-2} s^{-1}.

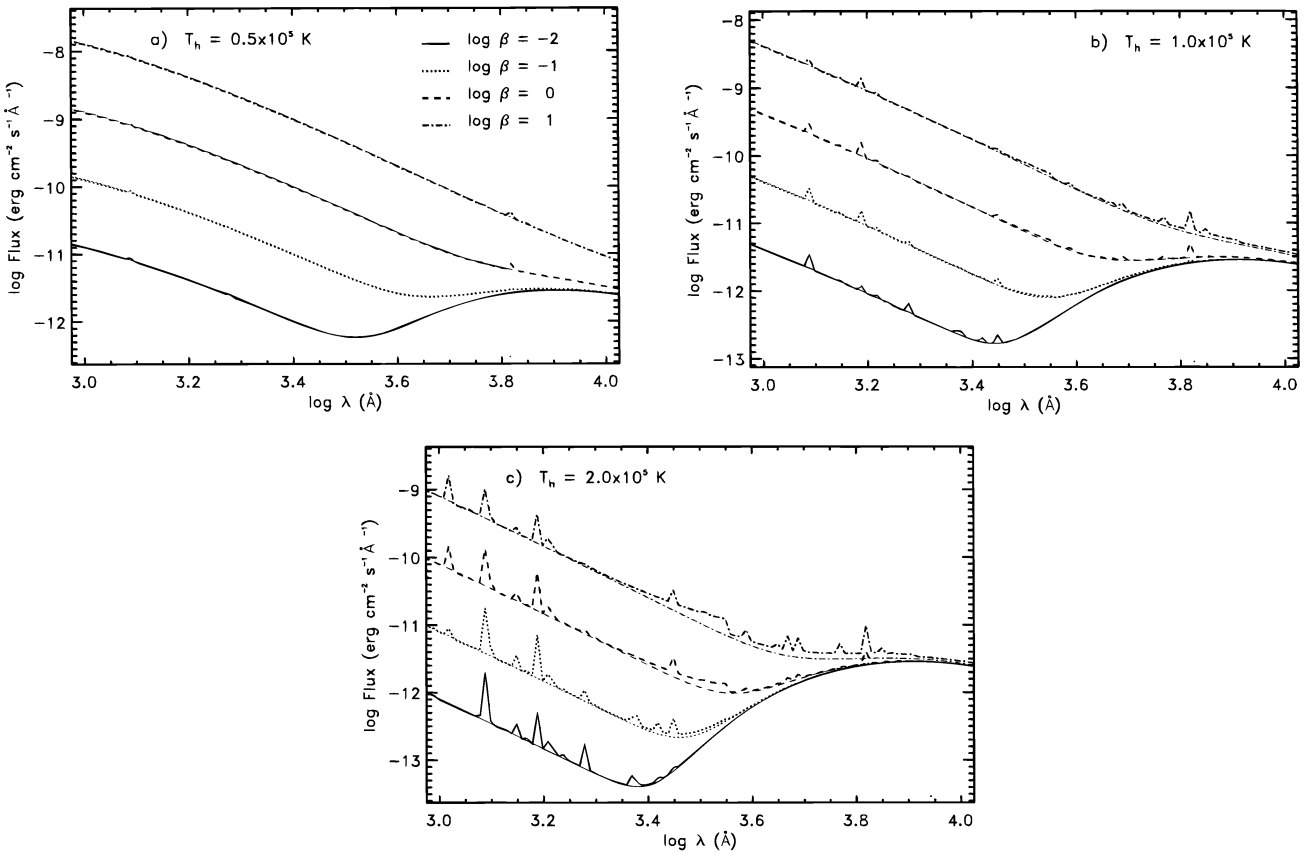

FIG. 5.—Blackbody flux curves for a binary without illumination (*thin lines*) and model spectra (*thick lines*) for different β and T_h = (*a*) 0.5, (*b*) 1.0, and (*c*) 2.0 × 10^5 K. We assumed a distance of 1 kpc as in Fig. 4.

to the continuum as L_h increases. The optical lines increase gradually in prominence as L_h increases because these lines must overcome the redgiant spectrum to become visible.

Figure 6 shows how illumination changes the broadband magnitudes of our model binary. In all cases, the magnitude difference—ΔU, ΔB, ΔV, and ΔK—between the illuminated and nonilluminated hemisphere is small, $\Delta K \lesssim \Delta V \lesssim \Delta B \lesssim \Delta U \lesssim 0.3$ mag. Low-luminosity and low-temperature hot components, $L_h \lesssim 6.2 \times 10^3\ L_\odot$ and $T_h \lesssim 0.5 \times 10^5$ K, produce no obvious change in broadband magnitudes, with $\Delta U \lesssim 0.03$ mag at all temperatures. These hot components emit few ionizing photons; the ionized portion of the red giant atmosphere is always small. At $L_h \sim 6.2 \times 10^3\ L_\odot$, for example, the total hot component flux intercepted by the red giant is only 5% of the red giant flux. If the red giant could emit all this flux in the optical and UV continuum, its effective temperature would be 3644 K instead of 3600 K, independent of T_h (eq. [B9]). The thin dotted line in Figure 6 plots magnitude differences between red giant hemispheres with effective temperatures of 3644 K and 3600 K. The classical reflection effect is significantly larger than the non-LTE reflection effect for all bands. However, classical illumination models do not vary with T_h as in non-LTE models.

The variation of line fluxes with T_h and L_h depends on both the ionization state and the type of transition (Figs. 7–8; Table 3). At low T_h, all fluxes increase rapidly with T_h due to the increase in ionizing photons. As T_h increases, the line fluxes no longer increase—or may even decrease—when the radiation field ionizes the element to the next state. In general, the line fluxes are simply proportional to L_h. The intercombination lines, however, have a relatively low critical density, $\sim 10^9$–10^{10} cm^{-3}, compared to the mean density in our models, $\sim 10^{10}$–10^{11} cm^{-3} (see Fig. 12). Collisional de-excitation is very important at these high densities and significantly reduces the fluxes of C III λ1908, Si III] λ1892, and other intercombination lines. The fluxes of these lines thus increase very slowly with L_h. Collisional de-excitation does not modify permitted lines significantly; these fluxes increase roughly linearly with L_h.

Although line fluxes provide a good comparison between our models and observations, equivalent widths better discriminate models that produce symbiotic spectra (see Table 4). Figure 9 shows equivalent widths (EWs) for emission lines from Figure 7. In general, the EWs of UV lines increase with T_h at any L_h because the line flux increases and the continuum flux decreases. The EWs of lower ionization species, such as O III] λ1664, are fairly independent of L_h due to the simple proportionality between line flux and L_h (see Fig. 7). The EWs of higher ionization lines, such as He II λ1640 and N V λ1240, increase as L_h, and the emission measure, increase. The optical spectra have a different behavior. The constant red giant flux dominates the optical continuum for nearly all T_h and L_h. Optical EWs thus increase with T_h. The Paschen continuum contributes a noticeable flux in our highest temperature models; most He I lines thus decrease with L_h for $T_h = 2.0 \times 10^5$K (see also Figure 5*c*).

The flux ratios of various emission lines also show interesting variations with T_h and L_h (Figs. 10–11). The Balmer lines are good examples. The $I(\mathrm{H}\alpha)/I(\mathrm{H}\beta)$ intensity ratio is a strong function of density and optical depth at high den-

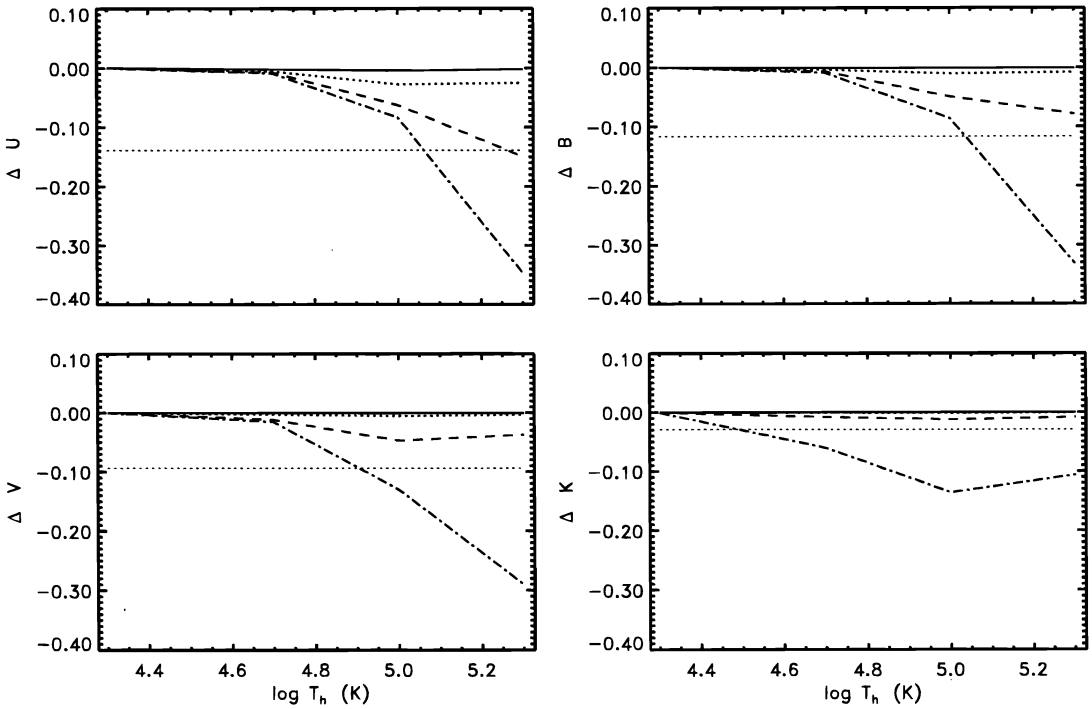

FIG. 6.—Differences in broadband magnitudes between opposite hemispheres of an illuminated red giant as a function of T_h. The four thick curves indicate differences for non-LTE model parameters in Fig. 5 (log $\beta = -2, -1, 0$, and 1). The thin dotted horizontal line plots magnitude differences for an LTE model in which the two red giant hemispheres have effective temperature of 3644 and 3600 K.

sities (Cox & Mathews 1969; Netzer 1975; Drake & Ulrich 1980). Collisions and self-absorption then redistribute level populations from their standard case B values. Our $I(\mathrm{H}\alpha)/I(\mathrm{H}\beta)$ initially increases with L_h at all T_h due to the increase in $\tau_{\mathrm{H}\alpha}$ with increasing density. The ratio then decreases with L_h once the density reaches $\sim 10^{11}$ cm^{-3}, because collisional de-excitation is important at high densities. Netzer (1975) and Drake & Ulrich (1980) found similar variations

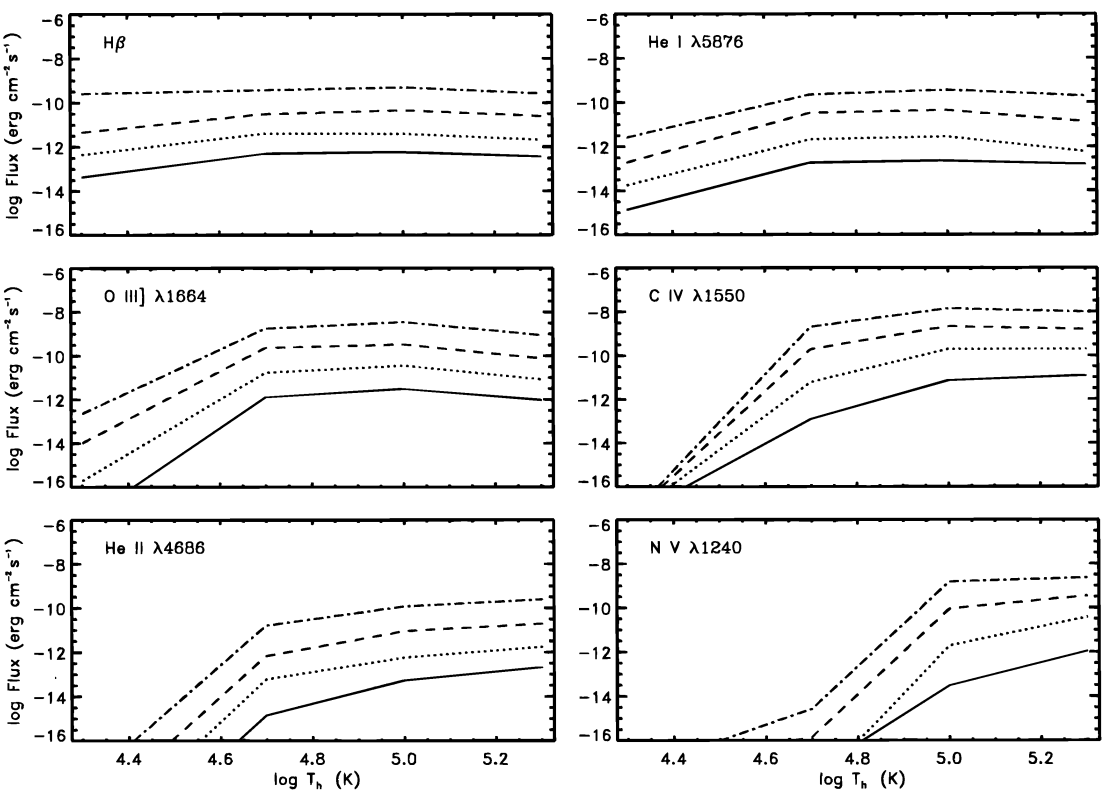

FIG. 7.—Model line fluxes of several optical and UV lines as functions of T_h for log $\beta = -2$ (*solid curves*), -1 (*dotted curves*), 0 (*dashed curves*), and 1 (*dot-dashed curves*). All line fluxes increase with increasing L_h; most line fluxes also increase with increasing T_h.

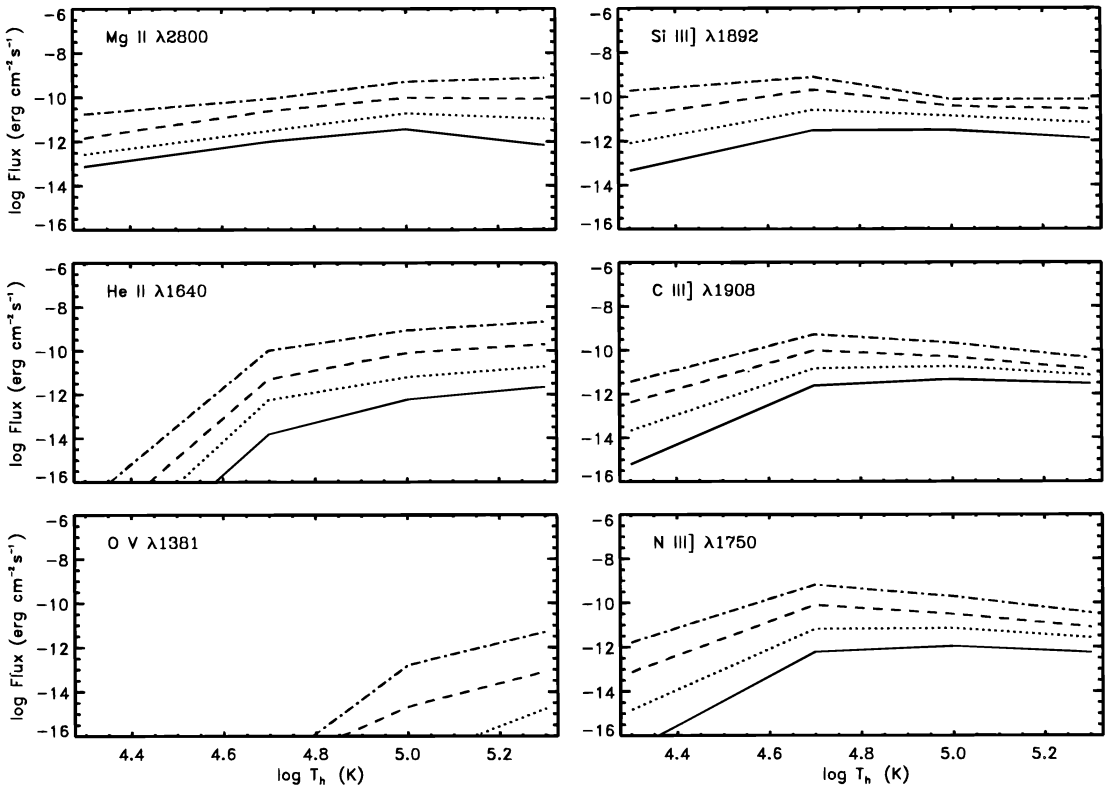

FIG. 8.—Comparison between permitted and intercombination model line fluxes as functions of T_h for log $\beta = -2$ (*solid curves*), -1 (*dotted curves*), 0 (*dashed curves*), and 1 (*dot-dashed curves*). Fluxes of intercombination lines increase more slowly with L_h than do permitted lines. Collisional de-excitation reduces intercombination line fluxes relative to permitted lines as L_h increases.

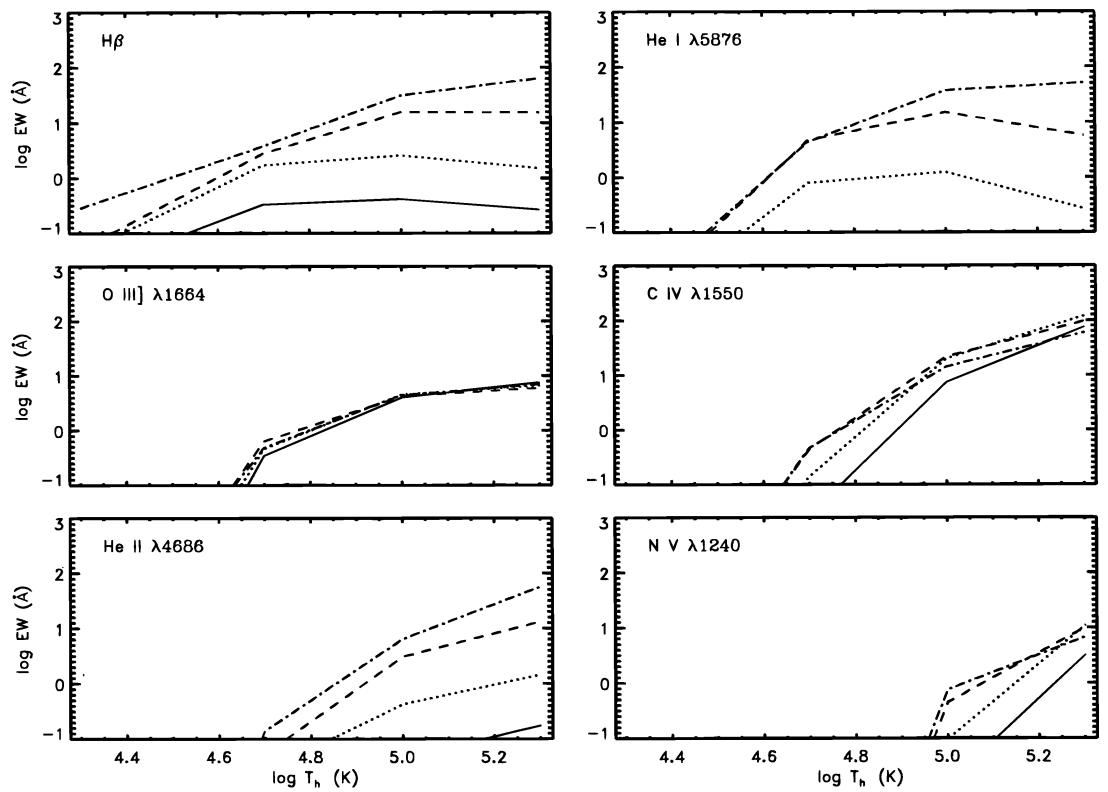

FIG. 9.—Equivalent widths (EWs) for emission lines from Fig. 7 as functions of T_h for log $\beta = -2$ (*solid curves*), -1 (*dotted curves*), 0 (*dashed curves*), and 1 (*dot-dashed curves*). All EWs increase in general with T_h; most EWs increase with L_h, although some, such as O III] λ1664, do not increase with L_h.

TABLE 4

LOGARITHM OF MODEL EMISSION-LINE EQUIVALENT WIDTHS (EWs)[a]

A. H, He LINES

L_h ($L_\odot$)	β	T_h (10^5 K)	Hα	Hβ	Pα	He I λ3889	He I λ4471	He I λ5876	He I λ6678	He I λ7065	He I λ10830	He II λ1640	He II λ4686
6.2×10^2.....	0.01	0.2	−1.3	−1.7	−1.9	−3.2	−3.7	−3.3	−4.0	−3.7	−2.0	−10.3	−10.7
	0.01	0.5	−0.2	−0.5	−0.8	−0.6	−1.3	−1.1	−1.9	−1.5	0.1	−2.4	−3.0
	0.01	1.0	0.0	−0.4	−0.6	−0.4	−1.1	−1.0	−1.8	−1.4	0.1	−0.2	−1.3
	0.01	2.0	0.0	−0.6	−0.6	−1.0	−1.3	−1.1	−2.1	−1.8	−0.3	1.2	−0.8
6.2×10^3.....	0.1	0.2	−0.6	−1.4	−0.9	−3.1	−3.4	−2.6	−3.2	−2.9	−1.1	−9.9	−10.0
	0.1	0.5	0.8	0.2	0.3	−0.2	−0.5	−0.1	−0.9	−0.5	1.0	−1.8	−1.6
	0.1	1.0	1.1	0.4	0.5	0.4	−0.1	0.1	−0.8	−0.3	1.1	−0.1	−0.4
	0.1	2.0	1.0	0.2	0.4	−0.1	−0.7	−0.6	−1.4	−1.0	0.5	1.1	0.2
6.2×10^4.....	1	0.2	−0.3	−1.3	0.0	−3.0	−3.3	−2.4	−2.9	−2.7	−0.7	−9.5	−9.6
	1	0.5	1.6	0.4	1.4	0.0	−0.2	0.7	−0.1	0.6	1.7	−1.9	−1.3
	1	1.0	2.0	1.2	1.6	0.9	0.6	1.2	0.3	0.9	1.9	0.0	0.5
	1	2.0	1.9	1.2	1.5	1.0	0.5	0.8	−0.2	0.3	1.6	1.2	1.1
6.2×10^5.....	10	0.2	0.3	−0.5	0.9	−3.0	−3.1	−2.3	−2.8	−0.7	−0.7	−8.9	−9.0
	10	0.5	1.5	0.6	1.9	0.0	−0.3	0.6	0.2	0.8	1.8	−1.6	−0.9
	10	1.0	2.3	1.5	2.2	1.0	0.8	1.6	1.3	1.7	2.3	0.0	0.8
	10	2.0	2.4	1.8	2.1	1.6	1.2	1.7	1.0	1.5	2.2	1.2	1.8

B. C, N LINES

L_h ($L_\odot$)	β	T_h (10^5 K)	C II λ1335	C II] λ2325	C III] λ1908	C IV λ1550	N II] λ2141	N III] λ1750	N IV] λ1486	N V λ1240
6.2×10^2.....	0.01	0.2	−2.7	−1.6	−4.1		−3.0	−5.6		
	0.01	0.5	−1.3	−0.3	0.0	−1.6	−1.9	−0.7	−2.7	
	0.01	1.0	−0.5	0.5	1.0	0.9	−1.2	0.2	−0.4	−1.8
	0.01	2.0	0.3	1.3	1.6	1.9	−0.4	0.7	0.5	0.5
6.2×10^3.....	0.1	0.2	−2.4	−1.5	−3.6		−2.9	−4.8		
	0.1	0.5	−1.7	−1.0	−0.2	−0.9	−2.6	−0.7	−2.1	−8.1
	0.1	1.0	−0.8	−0.1	0.6	1.3	−2.0	0.0	−0.1	−1.0
	0.1	2.0	−0.1	0.7	1.0	2.1	−1.3	0.4	0.5	1.0
6.2×10^4.....	1	0.2	−2.2	−1.6	−3.3		−2.9	−4.1		
	1	0.5	−1.7	−1.4	−0.4	−0.4	−3.2	−0.6	−1.8	−6.7
	1	1.0	−1.2	−0.9	0.0	1.3	−3.2	−0.3	−0.1	−0.3
	1	2.0	−0.5	−0.1	0.2	2.0	−2.5	−0.1	0.2	1.0
6.2×10^5.....	10	0.2	−2.0	−1.7	−3.3		−3.1	−3.7		
	10	0.5	−2.0	−2.2	−0.7	−0.3	−3.9	−0.7	−1.9	−6.5
	10	1.0	−1.4	−1.7	−0.4	1.2	−4.1	−0.5	0.0	−0.1
	10	2.0	−0.6	−1.0	−0.3	1.8	−3.5	−0.5	0.0	0.8

C. O, Mg, Si LINES

L_h ($L_\odot$)	β	T_h (10^5 K)	O III] λ1664	O IV] λ1403	O V] λ1218	O V] λ1371	O VI λ1043	Mg II λ2800	Si II] λ2335	Si III] λ1892	Si IV λ1397
6.2×10^2.....	0.01	0.2	−6.5					−1.7	−3.7	−2.2	−8.1
	0.01	0.5	−0.5	−3.7				0.1	−2.0	0.1	−1.3
	0.01	1.0	0.6	−0.4	−1.9	−7.6	−4.9	1.3	−0.9	0.8	0.2
	0.01	2.0	0.9	0.9	0.9	−4.6	−0.6	1.0	−0.2	1.2	0.9
6.2×10^3.....	0.1	0.2	−5.7					−2.2	−4.2	−2.0	−7.1
	0.1	0.5	−0.3	−4.2	−8.5			−0.4	−2.9	0.0	−0.8
	0.1	1.0	0.7	−0.2	−1.1	−6.3	−3.3	1.2	−1.8	0.5	0.2
	0.1	2.0	0.8	1.0	1.2	−3.1	0.9	1.6	−1.0	0.9	0.9
6.2×10^4.....	1	0.2	−4.9					−2.4	−4.7	−1.8	−6.2
	1	0.5	−0.2	−4.3	−9.3			−0.5	−3.6	−0.1	−0.4
	1	1.0	0.6	−0.1	−0.4	−4.8	−2.0	0.9	−3.3	−0.1	0.1
	1	2.0	0.8	0.8	1.4	−2.5	1.4	1.6	−2.3	0.6	0.6
6.2×10^5.....	10	0.2	−4.6					−2.4	−5.1	−1.6	−5.5
	10	0.5	−0.3	−4.4	−7.9			−0.9	−4.7	−0.5	−0.5
	10	1.0	0.7	−0.1	−0.1	−4.0	−1.3	0.6	−4.9	−0.8	0.0
	10	2.0	0.8	0.6	1.4	−1.7	1.5	1.5	−3.7	0.0	0.5

NOTE.—Blank spaces mark EWs practically equal to zero.

[a] In units of Å.

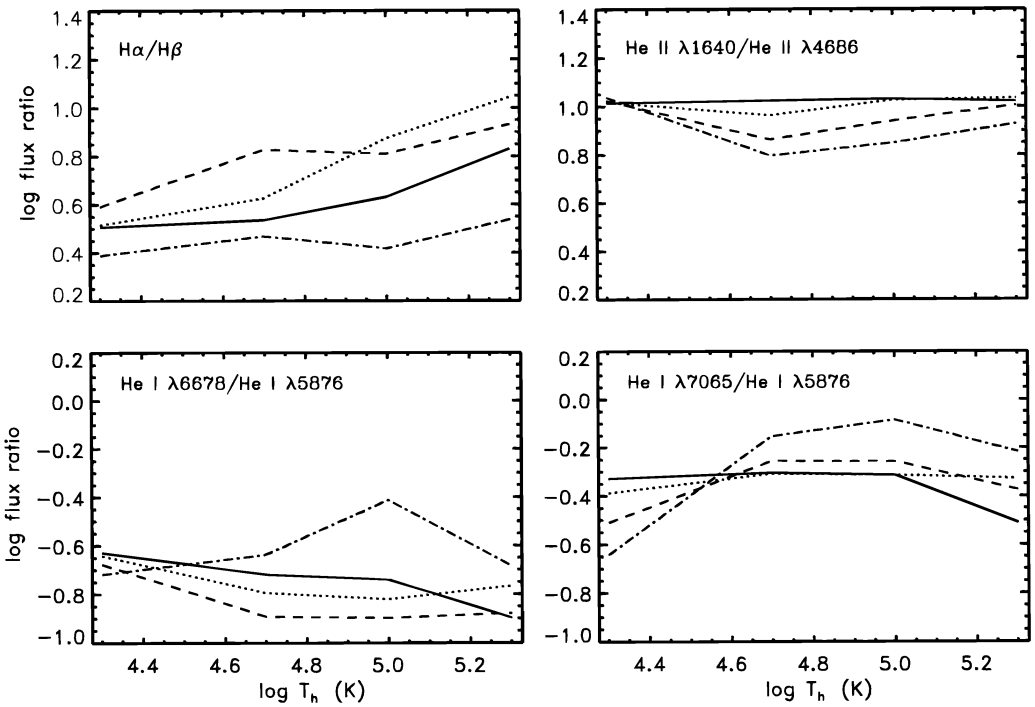

FIG. 10.—H and He emission-line flux ratios as functions of T_h for log $\beta = -2$ (*solid curves*), -1 (*dotted curves*), 0 (*dashed curves*), and 1 (*dot-dashed curves*).

and a similar range in $I(\mathrm{H}\alpha)/I(\mathrm{H}\beta)$ in calculations for active galactic nuclei and planetary nebulae.

The He I line ratios are also quite complicated functions of physical parameters (e.g., Clegg 1987; Almog & Netzer 1989). The metastability of the 2^3S level complicates calculations of He I line emission; collisions and self-absorption from this level can enhance some lines and reduce others. Our line ratios for $I(\lambda6678)/I(\lambda5876)$ and $I(\lambda7065)/I(\lambda5876)$ rarely approach case B values for high density conditions (see Proga et al. 1994). The $I(\lambda7065)/I(\lambda5876)$ ratio always exceeds the case B value of ~ 0.1; $I(\lambda6678)/I(\lambda5876)$ lies below its case B value of ~ 0.3. This behavior is characteristic of He I at high densities and low optical depths (Proga et al. 1994, and references therein).

He II line ratios depend more directly on L_h. All the optical and UV He II lines are optically thin in our models. The line ratios thus depend only on the ionized emission measure, which increases with L_h. The $I(\lambda1640)/I(\lambda4686)$ ratio exceeds the low-density case B value of 7–8 at low L_h, because the He III region is very small. The ratio approaches the case B value as L_h increases. High densities prevent the ratio from actually reaching the case B value (see also Storey & Hummer 1995).

The H I and He II emission-line ratios are often used to derive the interstellar reddening in symbiotics and other binary systems (e.g., Mikołajewska et al. 1995). Illumination causes these ratios to deviate significantly from case B predictions in low- and high-density conditions. Reddening estimates thus require accurate knowledge of the density, temperature, and optical depth when illumination produces a significant amount of the emission-line flux in a symbiotic binary.

Intensity ratios for intercombination lines do not suffer from optical depth effects and thus provide more accurate measures of T_h and L_h. Figure 11 illustrates this behavior for several ratios using lines of successive ionization states. At low L_h, these line ratios are simply proportional to the number of photons that can produce the higher ionization state and thus increase with L_h. Collisional de-excitation reduces emission from the higher ionization state as L_h increases, and the flux ratio then increases more slowly with L_h. In some cases, the flux ratio is almost completely independent of L_h.

Figure 11, along with Figure 9, indicates that several lines or line ratios might provide good T_h diagnostics for the hot component. Our models produce very little C IV $\lambda1550$ flux for $T_h \lesssim 5 \times 10^4$ K and very little N V $\lambda1240$ flux for $T_h \lesssim 10^5$ K. The $I(\mathrm{C\ IV}\ \lambda1550)/I(\mathrm{C\ III}]\ \lambda1908)$ and $I(\mathrm{N\ V}\ \lambda1240)/I(\mathrm{N\ IV}]\ \lambda1486)$ ratios thus allow a reasonable temperature estimate for $T_h \lesssim 10^5$ K. The $I(\mathrm{O\ V}]\ \lambda1218)/I(\mathrm{O\ IV}]\ \lambda1403)$ ratio is also a fairly reliable T_h indicator if $\lambda1218$ can be separated from Lyα. These line ratios are somewhat sensitive to L_h, especially when L_h is small. The $I(\mathrm{O\ IV}]\ \lambda1403)/I(\mathrm{O\ III}]\ \lambda1664)$ ratio increases gradually with T_h and is almost independent of L_h.

Finally, Figure 12 shows mean parameters that describe the global physical conditions within the photoionized red giant atmosphere. Panels in the left column plot mean values for the complete atmosphere; panels in the right column plot values for the He II region. In both cases, the mean electron temperature, $\langle T_e \rangle$, increases with T_h and L_h. For the He II region, $\langle T_e \rangle$ decreases with temperature for $T_h \gtrsim 0.5 \times 10^5$ K. These models have a very small transition region between the He I and He III zones. This region lies almost at the same height as the H^+ recombination zone where the temperature drops substantially (see Fig. 2, top left panel). Although the mean electron density, $\langle n_e \rangle$, and the emission measure, $n_e^2 L$, increase with L_h, they are not sensitive to T_h. Ionizing photons penetrate more deeply into the red giant atmosphere as L_h increases; the density

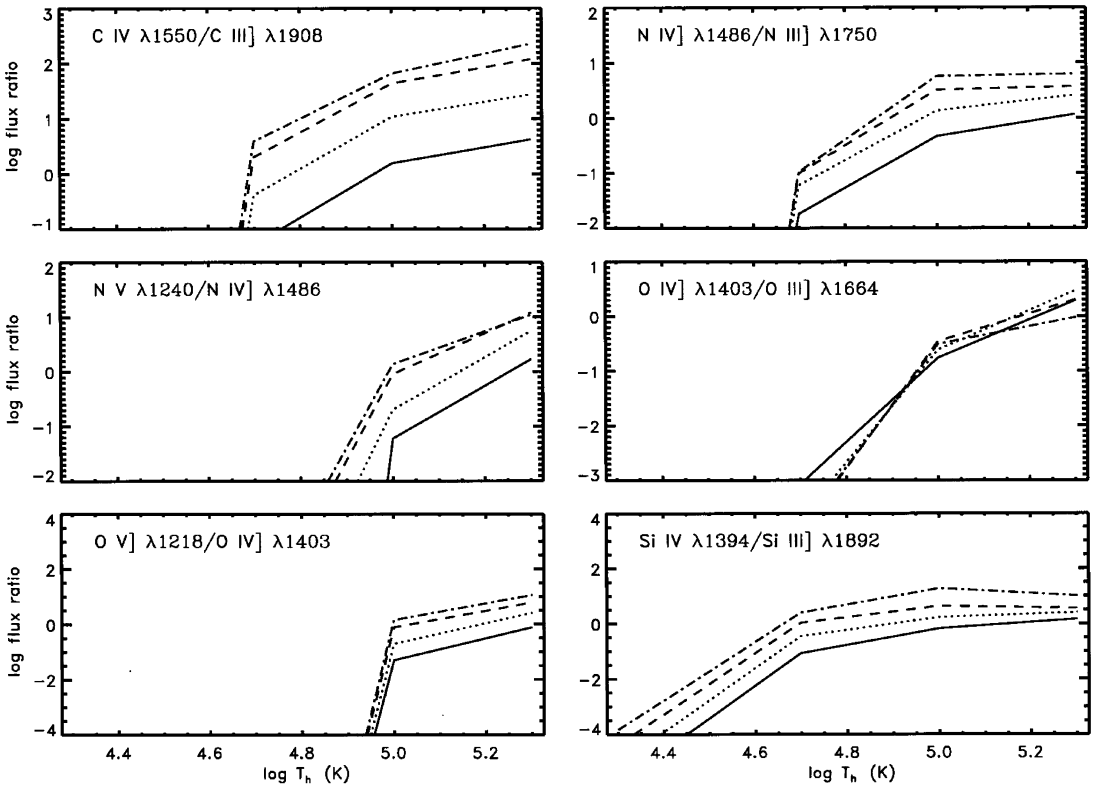

FIG. 11*a*

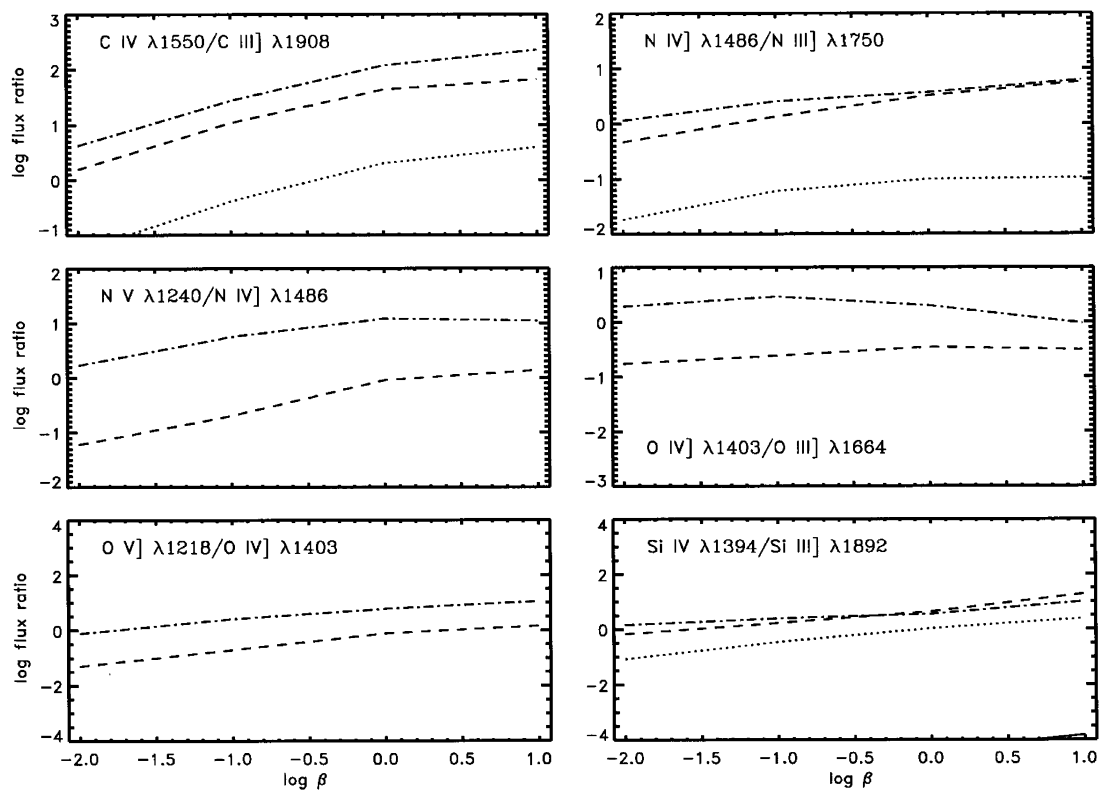

FIG. 11*b*

FIG. 11.—Emission-line flux ratios for metallic ions. (*a*) Line ratios as functions of T_h for log $\beta = -2$ (*solid curves*), -1 (*dotted curves*), 0 (*dashed curves*), and 1 (*dot-dashed curves*). (*b*) Line ratios as functions of β for $T_h = 0.5 \times 10^5$ K (*dotted lines*), $T_h = 1 \times 10^5$ K (*dashed lines*), and $T_h = 2 \times 10^5$ K (*dot-dashed lines*).

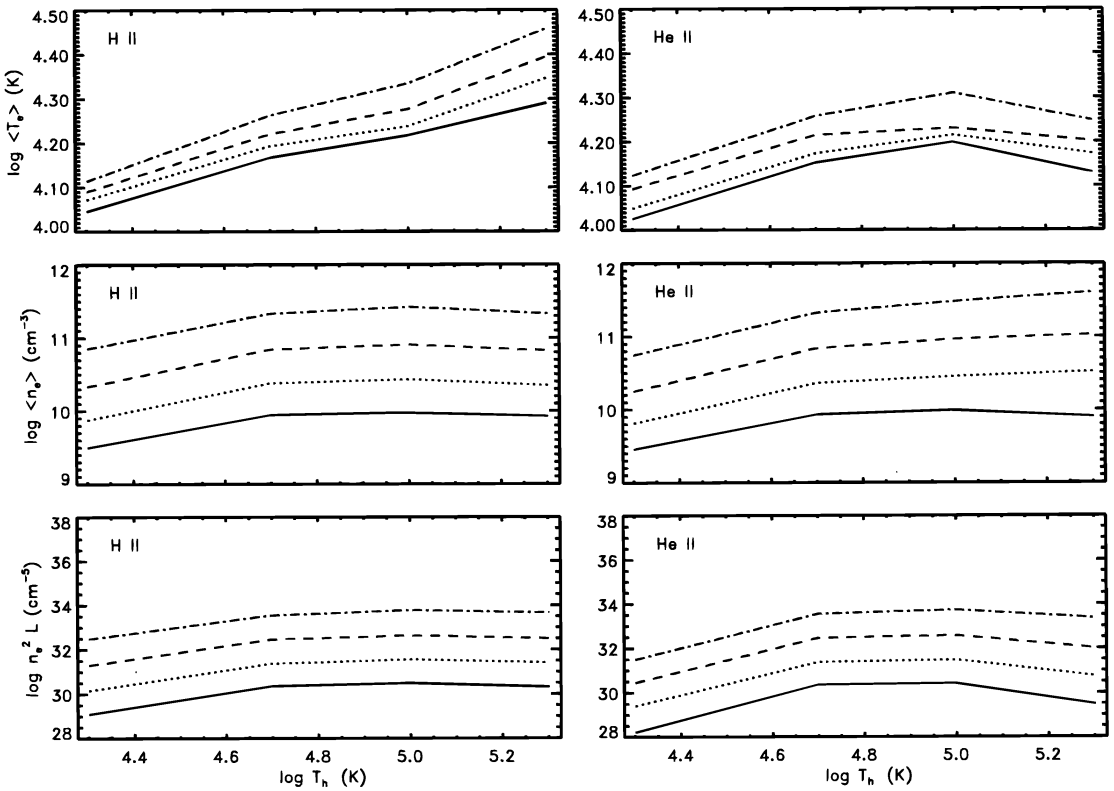

FIG. 12.—Mean parameters describing the global physical conditions within the photoionized red giant atmosphere as functions of T_h for log $\beta = -2$ (*solid curves*), -1 (*dotted curves*), 0 (*dashed curves*), and 1 (*dot-dashed curves*). Left panels plot mean values for the complete atmosphere; right panels plot values for the He II region.

increases with depth, so $\langle n_e \rangle$ and $n_e^2 L$ increase with L_h. For the He III region, the size and T_e increase with T_h. The density is lower in the He III region than the He II region because of the difference in electron temperature (see Fig. 2, top left and right panel). The lower density He III region then contributes more to $\langle n_e \rangle$ and $n_e^2 L$ with increasing T_h. Thus, the mean density and emission measure increase with temperature for $T_h \gtrsim 0.5 \times 10^5$ K and then flatten out because the He III region contribution is large. For the He II region, the mean density is lower for $T_h = 1 \times 10^5$ K than $T_h = 2 \times 10^5$ K at the lowest luminosity. The He II region is very small and coexists with the H^+ recombination zone, where the electron density has been reduced by hydrogen recombination.

2.4. *Limitations of Models*

Our atmospheric models have several simplifications that limit our ability to compare model results with actual observations. We adopt plane-parallel geometry and hydrostatic equilibrium, which is not appropriate for symbiotic red giants with massive, low-velocity winds (Seaquist, Taylor, & Button 1984; Taylor & Seaquist 1984; Nussbaumer & Vogel 1987). These models thus cannot reproduce the low-density emission observed in nearly all symbiotics. Although this restriction is important, our model yields a very useful measure of illumination in a red giant with little or no mass ejection. The plane-parallel and hydrostatic equilibrium assumptions are reasonable for such a giant and give us a strict lower limit for line fluxes produced by illumination (§ 2.1). We will consider the extra line flux produced in the wind in a separate paper.

We solve the radiative transfer problem with an escape probability approximation instead of solving the radiative transfer equations. There are many versions of this method (see Rybicki 1984) that have been used in a variety of applications (e.g., Kwan & Krolik 1981; Ferland & Mushotzky 1982; Hubbard & Puetter 1985; Ko & Kallman 1993). These approaches yield consistent results in some applications, such as the broad emission-line regions of quasistellar objects (see Netzer & Ferland 1984, and references therein). These techniques do not always agree with more detailed, and computer time intensive, methods that solve directly the radiative transfer equations (e.g., Avrett & Loeser 1988). More detailed approaches treat energy balance more accurately, for example, and thus they provide better estimates for cooling rates of very optically thick lines, such as Lyα. Avrett & Loeser (1988) show that line transfer effects with partial frequency redistribution can cause factor of 2 or more changes in hydrogen Balmer line fluxes and ratios. These modifications are important for detailed comparisons with observations. They are too small to change our main conclusion that hydrostatic illumination models fall far short of explaining observed line fluxes in typical symbiotic stars.

Our neglect of molecular opacity sources is another limitation of the model. Various molecules—including H_2O, TiO, CO, and H^-—are very important opacity sources in red giant atmospheres (e.g., Tsuji 1966, 1972). Although our approach treats the absorption of high-energy photons very accurately, the atmosphere does not absorb all the incident flux with wavelengths exceeding 912 Å. Thus, we do not consider cool, neutral layers in the red giant photosphere

and lower chromosphere. This region produces most of the strong absorption features and some weak emission lines (see Dupree 1986). The extra emission from a red giant chromosphere has little impact on our results; typical chromospheric fluxes are much weaker than lines observed in nearly all symbiotics (Kenyon 1986). The lack of red giant absorption features in our calculation prevents us from predicting variations in absorption-line strengths that could be compared with observations.

Finally, our calculation also underestimates the He I flux from the region where H II and He II recombine into H I and He I. We adopt a linear grid with constant Δz for this calculation, which limits our resolution of the H II recombination region. Due to zoning limitations, our line fluxes do not include radiation from the coolest part of the recombination region, which might contribute substantially to the He I emission. Experiments with finer zones show an increase in line fluxes and τ_{3889}, which indicates that better spatial resolution would improve our ability to model He I flux ratios in actual systems. Real improvements in our ability to model He I more accurately require H^- and other molecular opacities to derive an accurate density and temperature structure where the ionization fraction is small. This calculation is beyond the scope of this paper.

2.5. *Comparison with Observations*

Our model spectra display continuum and line emission that qualitatively resemble a symbiotic star spectrum. High-luminosity models have pronounced Balmer emission jumps and modest Paschen continua, as observed in many symbiotic stars (Allen 1984; Kenyon 1986). High-temperature models also have a rich emission-line spectrum from a wide variety of ionization states, which is also characteristic of symbiotic stars. The lowest temperature models, $T_h \lesssim 50{,}000$ K, fail to produce any of these features independent of L_h and are poor symbiotic models.

The illumination models account for several other observed parameters characteristic of symbiotic stars. Most well-studied symbiotics have $T_e \sim 10$–20×10^3 K and $n_e \sim 10^9$–10^{11} cm^{-3} (Kenyon 1986; Nussbaumer & Stencel 1987; Proga et al. 1994, and references therein). These estimates fall at or slightly below our model results. The mean electron temperature is not a good diagnostic because any photoionized nebula with solar abundances will have $T_e \sim 10^4$ K (e.g., Keenan & Aggarwal 1990; Kwan & Krolik 1981). The mean density and emission measure are better diagnostics. Most symbiotics have ionized nebulae with sizes comparable to the binary separation, $A \sim 1$–3 AU; $n_e^2 L \sim 10^{33}$–10^{34} cm^{-5} is characteristic of these systems and lies above most of our model results (Fig. 12).

Despite some successes, our illumination models fail to reproduce several basic observations of symbiotic stars due to the small angular size of the red giant. All symbiotics have very intense optical H I lines, with EW(Hβ) $\gtrsim 10$ Å. Most systems have EW(Hβ) > 100 Å (Allen 1980, 1984). Our models have EW(Hβ) ~ 1–10 Å and only approach EW(Hβ) $\gtrsim 50$ Å at unreasonably high luminosities (Fig. 9). This problem is worse for higher ionization lines. Our EW for He II λ4686 rarely exceeds 10 Å; the EW for N V λ1240 *never* exceeds 10 Å. Both lines are very intense features on most symbiotic spectra, with EW $\gtrsim 20$–50 Å (Kenyon 1986; Mürset et al. 1991; and references therein).

Our models also fail to explain typical He I line ratios. Many symbiotics have $I(\lambda 6678)/I(\lambda 5876) \gtrsim 0.5$ and $I(\lambda 7065)/I(\lambda 5876) \sim 0.6$–$1.2$. Our models produce reasonable $I(\lambda 7065)/I(\lambda 5876)$ ratios but usually have $I(\lambda 6678)/I(\lambda 5876) < 0.25$ (Fig. 10). The lack of λ6678 emission is due to the small height of our hydrostatic atmosphere. Proga et al. (1994) show that the observed He I line ratios require high densities $n_e \sim 10^{10}$ cm^{-3}, and very large optical depths in the λ3889 line, $\tau_{3889} \sim 100$–1000 (see also Schmid 1989). The path length through the ionized region must than be ~ 0.1–1 AU, which is a factor of ~ 100 larger than our $z_{\rm top} \sim 1$–2×10^{11} cm. A better treatment of the H II recombination region including molecular opacities, is needed to predict He I fluxes more accurately (§ 2.4).

To provide a better comparison of models with observations, we consider AG Peg as a specific example of a symbiotic star with an illumination spectrum. This system is a detached binary with a hot white dwarf companion to a fairly normal red giant star (e.g., Kenyon et al. 1993, and references therein). The optical continuum varies by ~ 0.3 mag in phase with the orbital radial velocity curve. Maximum light coincides with spectroscopic conjunction and with a maximum in the number and intensity of Fe II and [Fe II] emission lines (e.g., Merrill 1959; Belyakina 1968a, 1968b, 1970). Until 1985, the hot component resembled a Wolf-Rayet star, with broad He II and N V lines indicating outflow velocities of ~ 1000 km s^{-1}. These lines nearly disappeared in 1985 and were replaced by narrow features having velocity widths of 50 km s^{-1} or less (Kenyon et al. 1993; Vogel & Nussbaumer 1994). High signal-to-noise spectra continue to indicate a weak high-velocity wind from the hot component, but most of the emission lines are now produced in low-velocity material (Nussbaumer, Schmutz, & Vogel 1995). Kenyon et al. 1993 (see also Nussbaumer et al. 1995) show that the narrow features form in high-density gas close to the red giant photosphere. This system thus provides a good comparison for our models.

Figure 13 compares observations of AG Peg with model line fluxes from Figure 7 for $T_h = 10^5$ K and various L_h. We adopt an 800 pc distance and correct observed fluxes for a modest reddening, $E_{B-V} = 0.1$ (Kenyon et al. 1993). The observed optical and UV lines correspond to photometric phases of 6.97 and 7.05, respectively, when the hot component wind is very weak (Kenyon et al. 1993). The illuminated red giant atmosphere is completely in view at this phase. Kenyon et al. (1993) estimate $L_h \sim 600\ L_\odot$, $T_h \sim 10^5$

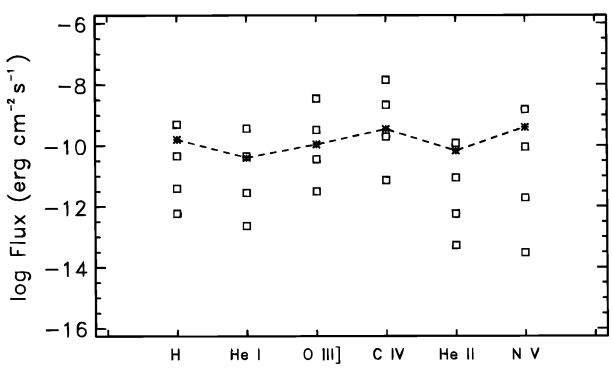

FIG. 13.—Comparison of model line fluxes from Fig. 7 and observations for AG Peg. Open squares show model fluxes for $T_h = 10^5$ K, a distance of 1 kpc, and log $\beta = -2$, -1, 0, and 1. At each ion, β increases with increasing line flux. The stars connected by the dashed line indicate observations at $d = 1$ kpc corrected for reddening $E(B-V) = 0.1$ mag.

K, $L_g \sim 1150\ L_\odot$, $T_g \sim 3650$ K, and $A = 2.5$ AU. These parameters imply that $R_g \sim 85\ R_\odot$ and $\beta \approx 0.013$. The model with $L_h = 6.2 \times 10^2\ L_\odot$ and $T_h \sim 10^5$ K is then the most suitable comparison for AG Peg. This model appears as the lowest set of boxes in Figure 13.

Our model fails to reproduce observations of AG Peg. All predicted line fluxes fall well below observed fluxes. The optical H I and He I lines are too low by factors of 200–300; higher ionization He II and N V lines are underpredicted by factors of 10^3–10^4. The O III] and C IV lines are in the best agreement with the data, although they are still too low by factors of 40–50. These results are expected because the red giant does not intercept a large enough fraction of hot component photons (§ 2.1).

We could bring our model predictions into better agreement with the data by increasing the angular size of the red giant (§ 2.1). Although there is little evidence that the red giant in AG Peg fills its Roche lobe (Kenyon et al. 1993), the red giant does have a substantial stellar wind. Seaquist & Taylor (1992) estimate $\dot{M} \sim 10^{-7}\ M_\odot\ \mathrm{yr}^{-1}$ from millimeter and centimeter radio observations. This wind effectively absorbs all H-ionizing photons inside a region with $R/A \sim 0.5$–1, depending on the velocity law (see Vogel 1991). Although we cannot accurately scale our hydrostatic solutions to a red giant with a low-velocity wind, a hydrostatic model with an effective $R_g/A \sim 1$ would increase our predicted fluxes for AG Peg by a factor of roughly 40. This simple scaling brings our model into agreement with observations for lines of intermediate ionization, such as O III] and C IV.

3. DISCUSSION

All true quiescent symbiotic stars have a red continuum and absorption features of a late-type giant (spectral type K or M), a weak blue continuum, and bright H I and He I emission lines. Many quiescent systems also have strong optical emission from He II, [O III], [Ne V], and [Fe VII]. In the ultraviolet, low-ionization intercombination lines—C III], N III], and O III]—are always present; higher ionization emission from He II, C IV, and N V is visible in the hottest systems. As we noted above, these emission lines form in high-density regions, $n_e \sim 10^6$–10^{11} cm^{-3}, with relatively low electron temperatures, $T_e \sim 1$–2×10^4 K (e.g., Nussbaumer & Stencel 1987; Proga et al. 1994, and references therein).

Three classes of models currently attempt to explain emission features in symbiotic stars. Two rely on the hot component to photoionize high-density gas and differ only on the *location* of ionized material in the binary system. In the standard photoionization model, the hot component ionizes material in the red giant wind to produce a large H II region surrounding the entire binary system. The hot component may eject material in its own wind, although this extra mass loss is often a small perturbation on the red giant wind (see below). This model successfully explains the millimeter and centimeter radio emission observed in most symbiotic stars and indicates red giant mass-loss rates of $\sim 10^{-7}\ M_\odot\ \mathrm{yr}^{-1}$ (e.g., Seaquist et al. 1984; Seaquist & Taylor 1990, 1992). In the D-type (dusty) symbiotics with Mira variables, most emission lines form in the low-density H II region with higher ionization lines produced in higher density gas closer to the hot component (e.g., Nussbaumer & Vogel 1987). In S-type (stellar) symbiotics with normal red giant primaries, radio emission and low ionization forbidden lines, such as the optical [O III] lines, form in low-density regions; the remaining lines form in high-density gas surrounding the hot component (e.g., Kenyon et al. 1993; Dobrzycka et al. 1993; Mikołajewska et al. 1995).

Illumination models place some of the emission in high-density material close to the red giant photosphere, as described in previous sections. In most cases, the hot component provides the energy to ionize portions of the red giant atmosphere (e.g., Pesce, Stencel & Oliversen 1987; Munari 1988; Munari & Renzini 1992), although Friedjung, Stencel, & Viotti (1983) proposed rotation as an energy source. If the heated atmosphere expands sufficiently, the mass-loss rate from the red giant might increase (e.g., Kenyon & Gallagher 1983; Pesce et al. 1987; Munari & Renzini 1992). This increased mass-loss rate could produce a more luminous hot component and additional illumination. Munari & Renzini (1992) suggested that illumination heating might be a self-regulating process and influence the long-term evolution of the red giant.

Colliding wind models produce line and continuum emission where the high-velocity, low-density wind from the hot component interacts with the dense, low-velocity red giant wind (Wallerstein et al. 1984; Willson et al. 1984; Kwok 1988, and references therein). The kinetic energy of the winds, instead of high-energy photons from the hot component, ionizes material in the interaction region; the roughly conical shape of this region explains line profiles in some symbiotics, such as HM Sge and V1016 Cyg (Wallerstein et al. 1984). This model may also explain the evolution of X-ray and radio fluxes in some outbursting systems (Willson et al. 1984; Kwok & Leahy 1984; Kwok 1988; Vogel & Nussbaumer 1994).

Our results indicate that illumination modifies the atmospheric structure of a hydrostatic red giant for conditions appropriate to symbiotic stars. Heating by energetic photons from the hot component causes the atmosphere to expand. The new density structure is, however, very flat, and it requires very little atmospheric expansion. We estimate that the illuminated atmosphere expands only by several percent for large L_h. Thus, the red giant mass-loss rate can increase due to illumination only if it fills or nearly fills its Roche lobe.

Illumination can also change the red giant mass-loss rate by modifying physical parameters of the wind acceleration region. Although the driving mechanism of red giant winds is not well known, most models involve acoustic or magnetic waves to deposit energy above the photosphere and then drive a wind (see Cuntz 1990; Rosner et al. 1991; and references therein). It is hard to predict how these mass-loss mechanisms respond to illumination without a detailed calculation, but published results indicate that illumination probably *decreases* the mass-loss rate in both acoustic and magnetic models. Acoustic models drive mass loss with long-wavelength waves (e.g., Cuntz 1990); these waves will deposit less energy in an atmosphere with a higher sound speed. Magnetic models drive mass loss with Alfvén waves. Our illuminated atmosphere has a very shallow density gradient (see Fig. 2). The Alfvén speed, $v_A \propto 1/\rho$, thus increases with radius much more slowly in an illuminated atmosphere than in a normal red giant atmosphere. This slow increase in v_A with radius should generate a lower mass-loss rate (see Rosner et al. 1991).

Illumination of a hydrostatic red giant produces very weak emission lines for conditions appropriate to symbiotic

binaries. Predicted line fluxes for these models are 40 to 10^4 times lower than observed in typical symbiotic stars. Moderate ionization lines, such as O III] and C IV, provide the best agreement with observations; low- and high-ionization features are much, much weaker than observations.

Our model produces weak high-ionization emission lines because a hydrostatic red giant in a typical symbiotic binary has a very small angular size. Many symbiotics have a large He III emission measure, $n_e^2 V \sim 10^{59}$ cm^{-3}, which requires a large nebular radius, R(He III) $\sim$ 0.1–1 AU, for observed densities of $n_e \sim 10^{10}$ cm^{-3} (e.g., Kenyon et al. 1993; Mikołajewska et al. 1995). With a vertical extent of only $\sim 10^{11}$ cm, our hydrostatic red giant atmosphere is too compact to achieve such large emission measures. A red giant with a more extended atmosphere would absorb more ionizing photons from the hot component and might reach observed emission measures. Our simple estimate in § 2.5 indicates that an illuminated wind model should explain fluxes of intermediate ionization emission features, such as O III] and C IV, in AG Peg. The H I, He II, and N V line fluxes in this system probably require a completely photoionized wind, which is also required to explain the radio fluxes and nebular morphology (e.g., Kenny, Taylor, & Seaquist 1991). We will consider wind models for red giants in our next paper.

Various constraints contribute to the low predicted fluxes for low-ionization emission lines such as H I and He I. First, our treatment of the H^+ recombination region causes us to underestimate line fluxes (§ 2.5). The small angular size of the hydrostatic atmosphere reduces line fluxes further below those needed to reproduce the observations (§ 2.1). Although better treatment of the H^+ recombination region and inclusion of an extended red giant atmosphere might solve our problem of low H I and He I fluxes, the unusual He I line ratios in many symbiotics may require an extra energy source to ionize or excite material (see the discussion in Kenyon et al. 1993). Collisions in interacting winds are an attractive possibility for this extra excitation. In addition to direct ionizations, collisional excitation allows less energetic photons with $\lambda > 912$ Å to ionize material in the outer red giant atmosphere. This region is also likely to have a higher density than in our hydrostatic models due to compression of the two winds. Long-wavelength photons are absorbed very close to the red giant photosphere in our hydrostatic models; additional recombination emission from a denser upper atmosphere would probably increase our predicted He I ratios. We will consider this possibility in a subsequent paper.

This work forms part of a doctoral dissertation presented at Nicolaus Copernicus Astronomical Center in Warsaw, Poland. We thank E. Avrett, R. Loeser, D. Sasselov, and H. Uitenbroek for helpful advice and comments. This project was partially supported by KBN Research Grants No. 2 P03D 015 09 and 2 P304 007 06, NASA grant NAG 5-1709, and the Smithsonian Institution's Predoctoral Fellowship Program.

APPENDIX A

We significantly modified Raymond's (1993; see also Raymond & Smith 1977) X-ray illumination code to calculate the structure of an illuminated red giant atmosphere. Our models assume a plane-parallel atmosphere in hydrostatic and radiative equilibrium. We adopt the same atomic models and rates as Raymond (1993), except for He I, where we use a 19 level atom to calculate singlet and triplet line fluxes more accurately (Proga et al. 1994). We also improve the radiative transfer calculation with a more accurate escape probability function and now calculate the escape probability at all continuum frequency points for H and He continua.

Our initial red giant atmosphere is based on the upper part of the LTE model from Brown et al. (1989) for $T_g = 3600$ K, $g = 10$ cm s^{-2}, and solar abundances (Anders & Grevesse 1989). This structure spans the height range $0 \le z \le 1.2 \times 10^{11}$ cm, which corresponds to $0.3 \ge \tau_{\rm Ross} \ge 2.3 \times 10^{-6}$ in Brown et al. We extend this model up to $z_{\rm top} = 1.99 \times 10^{11}$ cm using logarithmic extrapolation of the density and temperature as a function of z and divide the model into 200 layers distributed evenly in the geometrical height scale. Although this extrapolation probably does not reproduce accurately a real model atmosphere at low optical depths, the density iteration described below removes any artifacts associated with the extrapolated density law.

For a particular density structure, the calculation proceeds from the top down. We assume that the incident radiation is a plane-parallel beam and represent its spectrum by a blackbody with temperature T_h:

$$J_h(\nu) = \frac{L_h}{\sigma T^4} \frac{1}{4\pi(A - R_g)^2} B(\nu, T_h) . \tag{A1}$$

The incident flux per square centimeter of the red giant atmosphere at optical depth τ (measured normal to the surface) is

$$J_\theta^{\rm in}(\nu, z) = \cos\theta \exp\left[- \frac{\tau_c(\nu, z)}{\cos\theta} \right] J_h(\nu) . \tag{A2}$$

We neglect the red giant contribution to the photoionization of the gas because the effective temperature of the red giant is very low. All spectral and photoionization calculations use 500 logarithmically spaced bins covering photon energies 0.01 eV $\le h\nu \le$ 1 keV with an energy resolution $\log \delta(h\nu) = 0.01$.

For layer l at height z with thickness Δz, we use $n_{\rm H}(z)$ and the incident flux $J_\theta^{\rm in}(\nu, z)$ to iterate on the temperature and the ionization state of 12 elements. We iterate to achieve a thermal balance of 0.1% starting from the ionization state and temperature of layer $l + 1$. The ionization state and density give the opacity of photoionization continua and electron scattering at each photon energy; the incident radiation field is attenuated based on the optical depth along the incident ray, $\Delta z/\cos\theta$. The radiation emitted in layer l is computed from $n_{\rm H}(z)$, $T(z)$, and the ionization state. Compton scattering removes

photons from the incident beam and scatters them into the upward and downward beam but is negligible for this case. The vertically upward propagating rays also attenuate by a fraction corresponding to Δz as they pass through layer l. The calculation proceeds downward until 99% of the incident flux for $\lambda \leq 912$ Å has been absorbed. We define $z_{\rm bottom}$ as the lowest depth point in the illuminated atmosphere; the red giant atmosphere is undisturbed for $z < z_{\rm bottom}$.

Once the downward calculation of temperature and ionization state is complete, a new hydrostatic equilibrium calculation proceeds. The new density profile and the computed upward radiation flux, $J^u(v, z)$, are used for another iteration of the downward temperature and ionization calculation. The density converges to 1% in 20–100 iterations in most cases. Additional iterations change the density/temperature structure near the photosphere by less than 5%; the resulting spectrum also changes by less than 5%. We then add the radiation of the red giant photosphere to the upward propagating radiation field, $J^u(v)$. We assume a blackbody at temperature T_g for this component. The final one-dimensional model predicts the temperature and density structure with z and the line and continuum emission.

For H and He lines, we use the escape probability as the first-order approximation of the net radiative bracket, ρ, defined by the net radiative rate

$$n_j A_{ji} + n_j B_{ji} \bar{J}_{ji} - n_i B_{ij} \bar{J}_{ji} = n_j A_{ji} \rho_{ji} , \tag{A3}$$

where B_{ji} is the Einstein induced-emission rate and B_{ij} is the Einstein absorption rate. In the above formula, $\bar{J}_{ji} = \int_0^\infty \phi_v J_{ji}(v) dv$, where ϕ_v is the normalized profile function. The net radiative bracket can also be written as

$$\rho_{ji} = 1 - \bar{J}_{ji}/S_{ji} , \tag{A4}$$

where S_{ji} is the (frequency-independent) line source function:

$$S_{ji} = \frac{2hv^3}{c^2} \left(\frac{n_j}{n_i} \frac{g_i}{g_j} - 1 \right)^{-1} . \tag{A5}$$

For line transfer, we assume that the probability for a photon to escape the atmosphere is the probability that it is not self-absorbed. We neglect photoabsorption and Thomson scattering of line photons. These two processes are much less likely than self-absorption, and we feel this approach is valid considering other approximations made in this method. We use the escape probability formula from Kwan & Krolik (1981);

$$P^l_{\rm esc}(\tau_{ji}) = \begin{cases} 1 & \text{for } \tau_{ji} \leq 10^{-5} , \\ \dfrac{1 - \exp(-2\tau_{ji})}{2\tau_{ji}} & \text{for } 10^{-5} \leq \tau_{ji} < 1 , \\ 1 \Big/ \left\{ \tau_{ji} \pi^{1/2} \left[1.2 + \dfrac{0.5(\log \tau_{ji})^{1/2}}{1 + \tau_w/\tau_{ji}} \right] \right\} & \text{for } \tau_{ji} \geq 1 , \end{cases} \tag{A6}$$

where τ_w is the optical depth for which the line wings become optically thick. We assume $\tau_w = 10^5$ for all lines.

For other ions, each line connected to the ground state is treated in a two-level approximation:

$$n_1 n_e C_{12} = n_2 n_e C_{21} + N_2 A_{12} P^l_{{\rm esc},21} . \tag{A7}$$

The remaining lines are assumed to be optically thin.

We follow Ko & Kallman's (1993) approach to find the escape probability for a continuum photon:

$$P^c_{\rm esc}(\tau_{i\kappa}) = \begin{cases} 1 & \text{for } \tau_{i\kappa} < 1/\beta , \\ (\beta \tau_{i\kappa})^{-\beta/(\beta+1)} & \text{for } \tau_{i\kappa} \geq 1/\beta . \end{cases} \tag{A8}$$

In this expression, β is the power index in the approximate formula for the photoionization cross section:

$$\sigma_{i\kappa}(v) = \text{const} \times v^{-\beta} . \tag{A9}$$

For hydrogenic ions, $\beta = 3$. We include optical depth effects only for H and He continua.

In our approach, the escape probability for line and continuum photons is a function only of the optical depth, i.e., $P^l_{{\rm esc},ji} = P^l_{\rm esc}(\tau_{ji})$ and $P^c_{{\rm esc},i} = P^c_{\rm esc}(\tau_{i\kappa})$. The opacity of a line with lower i and upper j level at a given height at temperature T is

$$\kappa_{ji} = (n_i B_{ij} - n_j B_{ji}) \frac{hv_{ji}}{4\pi} \frac{1}{\Delta v_{\rm D}} , \tag{A10}$$

where $\Delta v_{\rm D}$ is the Doppler width

$$\Delta v_{\rm D} = \frac{v_{ji}}{c} \left(\frac{2kT}{Am_{\rm H}} \right)^{1/2} . \tag{A11}$$

The line optical depth at height z is then

$$\tau_{ji}(z) = \int_z^{z_{\rm top}} \kappa_{ji}(z) dz . \tag{A12}$$

The opacity of recombination photons for level i is

$$\kappa_{i\kappa}(\nu) = n_i \sigma_{i\kappa}(\nu) . \tag{A13}$$

The optical depth of continuum photons at height z is

$$\tau_{i\kappa}(\nu, z) = \int_z^{z_{\rm top}} \kappa_{i\kappa}(\nu, z) dz . \tag{A14}$$

The opacity and optical depth for free-free transitions are

$$\kappa_{\rm ff}(\nu) = 1.076 \times 10^{-70} Z^2 n_e n_Z T^{-1/2} (h\nu)^{-3} [1 - \exp(-h\nu/kT)] \bar{g}_{\rm ff} , \tag{A15}$$

and

$$\tau_{\rm ff}(\nu, z) = \int_z^{z_{\rm top}} \kappa_{\rm ff}(\nu, z) dz , \tag{A16}$$

where n_Z is the ion density, Z is the charge of the ion, and the $\bar{g}_{\rm ff}$ is the Gaunt factor taken to be 1. We consider free-free transitions only for hydrogen. Thus in equation (26), $Z = 1$ and $n_Z = n_p$, where n_p is the proton density. The last opacity source that we include in our calculation is Thomson scattering:

$$\kappa_{\rm T} = n_e \sigma_{\rm T} . \tag{A17}$$

This opacity is important only for very short wavelength photons.

The total optical depth from all continuum processes is then

$$\kappa_c(\nu) = \sum_m^{\rm element} \sum_k^{\rm ion} \sum_i^{\rm level} \kappa_{i\kappa}^{m,k}(\nu) + \kappa_{\rm ff}(\nu) + \kappa_{\rm T} . \tag{A18}$$

The continuum optical depth at height z is thus

$$\tau_c(\nu, z) = \int_z^{z_{\rm top}} \kappa_c(\nu, z) dz . \tag{A19}$$

APPENDIX B

The middle panel of Figure 1 shows our schematic picture of a symbiotic binary, in which a hot point source irradiates a spherical giant. We assume irradiation is constant in concentric annuli centered on the substellar point of the red giant surface as viewed from the hot component. For each concentric annulus, the hot component irradiates the red giant atmosphere at an angle θ with respect to the normal to the surface. The incident angle, θ, is the sum of two angles

$$\theta = \alpha + \phi , \tag{B1}$$

where

$$\phi = \tan^{-1}\left\{\frac{R_g \sin\alpha}{A - R_g \cos\alpha}\right\} . \tag{B2}$$

In this expression, α is the angle between the line connecting the centers of both stars and the line connecting the red giant center with the irradiated point; ϕ is the angle between the line connecting the centers of both stars and the line connecting the hot star with the irradiated point. Assuming that the incident flux is locally reradiated, the temperature of the irradiated point is

$$\sigma[T_g'(\alpha)]^4 = \sigma(T_g)^4 + \frac{L_h \cos\theta}{4\pi(A^2 + R_g^2 - 2AR_g \cos\alpha)} . \tag{B3}$$

The average temperature of the irradiated hemisphere, T_g' (or its effective temperature), is

$$2\pi R_g^2 \sigma(T_g')^4 = 2\pi R_g^2 \sigma(T_g)^4 + L_h f , \tag{B4}$$

where f is the fraction of L_h absorbed by the red giant. We calculate this fraction geometrically. The part of the illuminated hemisphere that can absorb radiation from the hot component is set by $\theta \leq 90°$. For $\theta = 90°$, the distance between the hot component and the irradiated point is

$$a_{\rm max} = (A^2 - R_g^2)^{1/2} . \tag{B5}$$

The fraction, f, is then equal to the ratio between the total surface area of a sphere with radius, $a_{\rm max}$, centered on the hot component, S_1, and the portion of this sphere that lies within the red giant photosphere, S_2:

$$f = \frac{S_2}{S_1} , \tag{B6}$$

where

$$S_1 = 4\pi a_{\max}^2 , \tag{B7}$$

and

$$S_2 = 2\pi a_{\max}(a_{\max} + R_g \cos \alpha_{\max} - A) . \tag{B8}$$

The angle $\alpha_{\max}$ is the value of α at the tangent point, $\theta = 90°$, and it is $\alpha_{\max} = \cos^{-1}(R_g/A)$. Thus, the average temperature is

$$(T_g')^4 = (T_g)^4 + L_h \frac{a_{\max} + (R_g^2/A) - A}{4\pi R_g^2 \sigma a_{\max}} . \tag{B9}$$

We define the representative angle, θ_r, as the incident angle for which

$$T_g'(\theta_r) = T_g' . \tag{B10}$$

This angle is

$$\frac{\cos \theta_r}{(A^2 + R_g^2 - 2AR_g \cos \alpha)} = \frac{a_{\max} + (R_g^2/A) - A}{R_g^2 a_{\max}} , \tag{B11}$$

using equations (B3) and (B9).

REFERENCES

Allen, D. A. 1980, MNRAS, 192, 521
———. 1984, Pub. Astron. Soc. Australia, 5, 369
Almog, Y., & Netzer, H. 1989, MNRAS, 238, 57
Anders, E., & Grevesse, N. 1989, Geochim. Cosmochim. Acta, 53, 197
Avrett, E. H., & Loeser, R. 1988, ApJ, 331, 211
Belyakina, T. S. 1968a, Izv. Krymskoi Astrofiz. Obs., 38, 171
———. 1968b, AZh, 45, 139
———. 1970, Astrofizika, 6, 49
Bowen, G. H. 1988, ApJ, 329, 299
Brett, J. M. 1989, MNRAS, 241, 247
Brett, J. M., & Smith, R. C. 1993, MNRAS, 264, 641
Brown, J. A., Johnson, H. R., Alexander, D. R., Cutright, L. C., & Sharp, C. M. 1989, ApJS, 71, 623
Catalán, M. S., Davey, S. C., Sarna, M. J., Smith, R. C., & Wood, J. 1994, MNRAS, 269, 879
Clegg, R. E. S. 1987, MNRAS, 229, 31
Cox, D. P. & Mathews, W. G. 1969, ApJ, 155, 859
Cuntz, M. 1990, ApJ, 353, 255
Dobrzycka, D., Kenyon, S. J., & Mikołajewska, J. 1993, AJ, 106, 284
Drake, S. A., & Ulrich, R. K. 1980, ApJS, 42, 351
Dupree, A. K. 1986, ARA&A, 24, 377
Ferguson, D. H., & James, T. 1994, ApJS, 94, 723
Ferland, G. J., & Mushotzky, R. F. 1982, ApJ, 262, 564
Friedjung, M., Stencel, R. E., & Viotti, R. 1983, A&A, 126, 407
Grauer, A. D., & Bond, H. E. 1983, ApJ, 271, 259
Gustafsson, B., Bell, R. A., Eriksson, K., & Nordlund, A. 1975, A&A, 42, 407
Gustafsson, B., & Jørgensen, U. G. 1994, A&A, Rev., 6, 19
Hubbard, E. N., & Puetter, R. C. 1985, ApJ, 290, 394
Jordan, C., & Linsky, J. L. 1987, in Exploring the Universe with the *IUE* Satellite, ed. Y. Kondo (Dordrecht: Reidel), 259
Keenan, F. P., & Aggarwal, K. M. 1990, ApJ, 350, 262
Kenny, H. T., Taylor, A. R., & Seaquist, F. R. 1991, ApJ, 366, 549
Kenyon, S. J. 1982, PASP, 94, 165
———. 1986, The Symbiotic Stars (Cambridge: Cambridge Univ. Press)
———. 1988, AJ, 96, 337
Kenyon, S. J., & Gallagher, J. S. 1983, AJ, 88, 666
Kenyon, S. J., Mikołajewska, J., Mikołajewski, M., Polidan, R. S., & Slovak, M. H. 1993, AJ, 106, 1573
Kenyon, S. J., & Webbink, R. F. 1984, ApJ, 279, 252
Ko, Y., & Kallman, T. R. 1993, ApJ, 431, 273
Kurucz, R. L. 1991, in Stellar Atmospheres: Beyond Classical Models, ed. L. Crivellari, I. Hubeny, & D. G. Hummer (NATO ASI Ser. C, 341) (Dordrecht: Kluwer), 441
Kwan, J., & Krolik, J. H. 1981, ApJ, 250, 478
Kwok, S. 1988, in IAU Colloq. 103, The Symbiotic Phenomenon, ed. J. Mikołajewska, M. Friedjung, S. J. Kenyon, & R. Viotti (Dordrecht: Kluwer), 129
Kwok, S., & Leahy, D. A. 1984, ApJ, 283, 675
Margon, B., Downes, R. A., & Katz, J. I. 1981, Nature, 293, 200
Merrill, P. W. 1959, ApJ, 129, 44
Mikołajewska, J., & Kenyon, S. J. 1992, MNRAS, 256, 177
Mikołajewska, J., Kenyon, S. J., & Mikołajewski, M. 1989, AJ, 98, 1427
Mikołajewska, J., Kenyon, S. J., Mikołajewski, M., Garcia, M. R., & Polidan, R. S. 1995, AJ, 109, 1289
Morgan, D. H. 1992, MNRAS, 258, 639
Munari, U. 1988, A&A, 207, L8
Munari, U., & Renzini, A. 1992, ApJ, 397, L87
Mürset, U., Nussbaumer, H., Schmid, H. M., & Vogel, M. 1991, A&A, 248, 458
Netzer, H. 1975, MNRAS, 171, 395
Netzer, H., & Ferland, G. J. 1984, PASP, 96, 593
Nordlund, A., & Vaz, L. P. R. 1990, A&A, 228, 231
Nussbaumer, H., Schmutz, W., & Vogel, M. 1995, A&A, 293, L13
Nussbaumer, H., & Stencel, R. E. 1987, in Exploring the Universe with the *IUE* Satellite, ed. Y. Kondo (Dordrecht: Reidel), 85
Nussbaumer, H., & Vogel, M. 1987, A&A, 182, 51
Osterbrock, D. E. 1989, Astrophysics of Gaseous Nebulae and Active Galactic Nuclei (Mill Valley: University Science Books)
Pesce, J. E., Stencel, R. E., & Oliversen, N. A. 1987, PASP, 99, 1178
Podsiadlowski, P. 1991, Nature, 350, 136L
Proga, D., Mikołajewska, J., & Kenyon, S. J. 1994, MNRAS, 268, 213
Raymond, J. C. 1993, ApJ, 412, 267
Raymond, J. C., & Smith, B. W. 1977, ApJS, 35, 419
Rosner, R., An, C.-H., Musielak, Z. E., Moore, R. L., & Suess, S. T. 1991, ApJ, 372, L91
Rybicki, G. B. 1984, in Methods in Radiative Transfer, ed. W. Kalkofen (Cambridge: Cambridge Univ. Press), 21
Schmid, H. M. 1989, in IAU Colloq. 122, Physics of Classical Novae, ed. A. Cassatella & R. Viotti (Berlin: Springer), 303
Seaquist, E. R., Krogulec, M., & Taylor, A. R. 1993, ApJ, 410, 260
Seaquist, E. R., & Taylor, A. R. 1990, ApJ, 349, 313
———. 1992, ApJ, 387, 624
Seaquist, E. R., Taylor, A. R., & Button, S. 1984, ApJ, 284, 202
Storey, P. J., & Hummer, D. G. 1995, MNRAS, 272, 41
Tavani, M., & London, R. 1993, ApJ, 410, 281
Taylor, A. R., & Seaquist, E. R. 1984, ApJ, 286, 263
Tsuji, T. 1966, PASJ, 18, 127
———. 1972, A&A, 23, 411
Vaz, L. P. R., 1984, Ph.D. thesis, Copenhagen Univ. Obs.
Vaz, L. P. R., & Nordlund, A. 1985, A&A, 147, 281
Vogel, M. 1991, A&A, 249, 173
Vogel, M., & Nussbaumer, H. 1994, A&A, 284, 145
Wallerstein, G., Willson, L. A., Salzer, J., & Brugel, E. 1984, 133, 1137
Willson, L. A., Wallerstein, G., Brugel, E., & Stencel, R. E. 1984, A&A, 133, 154
Yungel'son, L. R., Livio, M., Tutukov, A. V., & Kenyon, S. J. 1995, ApJ, 447, 656